© 2020. Published by The Company of Biologists Ltd | Journal of Cell Science (2020) 133, jcs242834. doi:10.1242/jcs.242834

TOOLS AND RESOURCES

Optimizing live-cell fluorescence imaging conditions to minimize phototoxicity

Alex Kiepas[1,2,*], Elena Voorand[2,3], Firas Mubaid[1], Peter M. Siegel[2,3,4,5] and Claire M. Brown[1,5,6,7,8,*]

ABSTRACT

Fluorescence illumination can cause phototoxicity that negatively affects living samples. This study demonstrates that much of the phototoxicity and photobleaching experienced with live-cell fluorescence imaging occurs as a result of 'illumination overhead' (IO). This occurs when a sample is illuminated but fluorescence emission is not being captured by the microscope camera. Several technological advancements have been developed, including fast-switching LED lamps and transistor–transistor logic (TTL) circuits, to diminish phototoxicity caused by IO. These advancements are not standard features on most microscopes and many biologists are unaware of their necessity for live-cell imaging. IO is particularly problematic when imaging rapid processes that require short exposure times. This study presents a workflow to optimize imaging conditions for measuring both slow and dynamic processes while minimizing phototoxicity on any standard microscope. The workflow includes a guide on how to (1) determine the maximum image exposure time for a dynamic process, (2) optimize excitation light intensity and (3) assess cell health with mitochondrial markers.

This article has an associated First Person interview with the first author of the paper.

KEY WORDS: Fluorescence microscopy, Phototoxicity, Cell migration, Mitochondrial dynamics, Microtubule dynamics, Adhesion dynamics

INTRODUCTION

Fluorescence microscopy provides a convenient, selective and sensitive way to observe living systems. Although modern microscopes are capable of capturing live-cell dynamics with incredible spatial and temporal resolution, phototoxicity has emerged as a significant limitation (Carlton et al., 2010; Laissue et al., 2017). Normally, fluorescent molecules absorb light energy and enter an excited state. A proportion of these excited fluorescent molecules can photobleach resulting in the production of singlet oxygen species during the imaging process (Stennett et al., 2014). It is generally thought that phototoxicity of live samples is tightly linked to the release of highly reactive oxygen species (ROS) during photobleaching (Laloi and Havaux, 2015).

Cells have several physiological mechanisms to deal with ROS production, including the induction of catalases, peroxidases and superoxide dismutases, the synthesis of antioxidants, and cell cycle delay (Thorpe et al., 2004). Under physiological conditions, most growing cells can successfully manage ROS generated by aerobic metabolism. Additional ROS generated by fluorescent illumination, however, may overwhelm enzymes and mechanisms typically in place to limit damage. In particular, the quantity of ROS production may affect the ability of cells to effectively detoxify ROS. Consequently, two general approaches have been proposed for reducing photobleaching and phototoxicity: (1) increasing the exposure time and decreasing excitation light power (diffuse light delivery; DLD); or (2) decreasing the exposure time and increasing excitation light power (condensed light delivery; CLD). Proponents of the former approach argue that generating lower doses of ROS over a longer period of time alleviates pressure on cellular mechanisms designed to eliminate ROS (Dixit and Cyr, 2003; Icha et al., 2017; Magidson and Khodjakov, 2013). Indeed, dye oxidation is reversible if cells are exposed to low irradiation levels (Dixit and Cyr, 2003). In contrast, proponents of the latter approach argue that photobleaching and phototoxicity depend on total light dose rather than exposure time (Douthwright and Sluder, 2017; Ettinger and Wittmann, 2014).

Thus, the goal of the present study is to provide a comprehensive workflow to minimize phototoxicity during live-cell fluorescence imaging and explore CLD and DLD approaches. Using cell migration and mitochondrial morphology as sensitive readouts of cell health, we demonstrate that 'illumination overhead' (IO) beyond the camera exposure time causes a significant amount of phototoxicity and photobleaching. This is especially significant under CLD conditions, when short exposure times with high light powers are employed. The results show that longer camera exposure times and stream acquisition can be implemented to circumvent the negative effects caused by IO without the need for specialized equipment. We use the microtubule tip-binding protein EB3 (also known as MAPRE3) to demonstrate how the maximum exposure time for a fast process, such as microtubule tip tracking ($0.5\ \mu m\ s^{-1}$) (Komarova et al., 2009; Stepanova et al., 2003), can be determined. Additionally, we show how the signal-to-noise ratio (S/N) of images can be improved through median filtering, spatial binning and temporal binning to access even lower illumination powers. Finally, using adhesion dynamics as an example, we demonstrate how the workflow can be used to detect often unobserved cellular processes and answer novel biological questions. Overall, the conclusion of the study is to maximize the image exposure time, avoid time delays between subsequent images, and minimize the light intensity to reduce the impact of IO and minimize phototoxicity.

[1]Department of Physiology, McGill University, Montreal, Canada, H3G 1Y6. [2]Goodman Cancer Research Centre, McGill University, Canada, H3G 1A1. [3]Department of Biochemistry, McGill University, Montreal, Canada, H3G 1Y6. [4]Department of Medicine, McGill University, Montreal, Canada, H4A 3J1. [5]Department of Anatomy & Cell Biology, McGill University, Canada, H3G 0B1. [6]Advanced BioImaging Facility (ABIF), McGill University, Montreal, Canada, H3A 0C7. [7]Cell Information Systems, McGill University, Montreal, Canada, H3G 0B1. [8]Centre for Applied Mathematics in Bioscience and Medicine (CAMBAM), McGill University, Montreal, Canada, H3G 1Y6.

*Authors for correspondence (alex.kiepas@mail.mcgill.ca; claire.brown@mcgill.ca)

P.M.S., 0000-0002-5568-6586; C.M.B., 0000-0003-1622-663X

Received 12 December 2019; Accepted 9 January 2020

Journal of Cell Science (2020) 133, jcs242834. doi:10.1242/jcs.242834

RESULTS

IO is a widespread problem in fluorescence imaging

The optimal method for reducing phototoxicity depends on the microscope hardware. For example, older bulb-based light sources need to warm up for ∼30 min before use (Baird et al., 2014) and cannot be repeatedly turned on and off. Thus, mechanical shutters are necessary to control sample illumination (Albeanu et al., 2008). Mechanical shutters require tens or hundreds of milliseconds to open and close (Wagenaar, 2012). Consequently, samples receive additional light exposure, termed 'illumination overhead' (IO), where the sample is exposed to light but fluorescence emission is not being captured by the detector.

Recent advancements in electronics engineering have essentially eliminated the need for physical shutters through the use of light sources that can be turned on and off electronically (e.g. LED light sources and solid-state lasers). Unfortunately, delays in camera initiation, unsynchronized light source activation, and software and data handling delays can still contribute to IO. Transistor-transistor logic (TTL) circuits can be implemented between the camera and light source to limit the 'on time' of the light source precisely to the camera exposure time. However, measuring IO, implementing TTL or minimizing IO in other ways can be technically challenging. Indeed, there is a general need to create awareness of the problem as a survey conducted by Canada BioImaging (CBI) of 14 light microscopy facilities and 41 facility users (from across Canada) revealed that 21% of facility managers and 51% of facility users were unaware of IO (Table S1). A further 43% of facility managers and 66% of facility users were unaware that IO could occur on the order of hundreds of milliseconds when mechanical shutters are used (Table S1). In addition, there are over 100 widefield microscopes in use in the facilities surveyed, and 65–70% of facilities rely on bulb-based light sources that require mechanical shutters and cannot take advantage of direct TTL triggering. Half of the facilities have one or more spinning disk (SD) confocal microscopes in use and 30% of facility users employ an SD microscope for their research.

TTL circuits can sometimes eliminate IO caused by hardware and software delays

Live-cell fluorescence imaging is commonly conducted on widefield, SD confocal or total internal reflection fluorescence (TIRF) microscopes (Frigault et al., 2009). There are several different ways of controlling fluorescence light delivery to samples on these platforms including shutters (bulb-based systems), USB software triggering of LED lamps or solid-state lasers, or a TTL circuit where electrical current is only sent to the light source when the camera is actively acquiring fluorescence photons (Fig. 1A). For USB triggering, careful synchronization between the light source and camera is required to avoid software delays in executing the command and saving acquired data that can contribute to IO.

In addition to light source activation, there are also two different methods of acquiring time-lapse data: interval imaging and stream acquisition (Fig. 1A). Interval imaging allows users to set a time delay between image acquisitions. Following each acquisition, the image is saved to the hard drive of the computer before the next image is captured. In contrast, stream acquisition attempts to capture images as quickly as possible (up to the camera frame rate) while the sample is constantly illuminated. Importantly, images can be temporarily stored on the random-access memory (RAM) of the computer to permit faster write speeds for rapid imaging.

Given this information, the total illumination time and IO were determined for an LED light source and several solid-state lasers using the imaging protocols outlined in Fig. 1A. Experiments with the LED light source were conducted on a widefield microscope that could be configured with a direct TTL trigger, a USB connection or a mechanical shutter. Measurements with an oscilloscope demonstrated that both TTL and USB control of the light source resulted in rapid on and off switching within less than half a millisecond (Fig. 1B). In contrast, the mechanical shutter required ∼10 ms to open and ∼10 ms to close (Fig. 1B). Next, the camera exposure time was set to 24 ms in the microscope image acquisition software and total sample exposure to light was measured as an image was captured with each configuration. Although TTL and USB triggered the light source in almost exactly the same amount of time, only the TTL trigger was accurate in limiting the total exposure time of the sample to precisely 24 ms (Fig. 1C). In fact, the total exposure time delivered with the USB configuration (137 ms) was almost six times longer than the desired exposure time (Fig. 1C). Image acquisition with the mechanical shutter was almost 10 times longer than the exposure time (230 ms) (Fig. 1C).

Similar experiments were conducted on an SD confocal microscope with solid state lasers. The SD microscope was configured so that laser intensity and shuttering were regulated by an acousto-optic tunable filter (AOTF) controlled by the microscope image acquisition software connected through a USB cable. The activation and deactivation times for the lasers were found to be less than 0.5 ms and independent of the laser line (Fig. 1D). The total illumination time was measured and, for a 100 ms exposure time, stream acquisition added ∼17 ms of IO, while interval imaging added ∼42 ms (Fig. 1E).

Total light dose determines photobleaching and phototoxicity

Several studies report that longer exposure times coupled with lower light intensities (DLD), improve cell health (reviewed in Icha et al., 2017). Therefore, photobleaching and phototoxicity were measured in response to different exposure times.

An optical power meter was used to measure incident light intensity at the focus of the imaging lens. Camera exposure times were scaled with illumination power to maintain a constant number of photons during image acquisition (Table S2). Chinese Hamster Ovary K1 (CHO-K1) cells stably expressing paxillin–EGFP were seeded onto fibronectin-coated glass coverslips, allowed to adhere and grow overnight, and then fixed with paraformaldehyde (PFA). Samples were left in PBS supplemented with sodium azide to avoid bacterial growth. Fixed cells were imaged with a 20×0.8 NA objective lens on the widefield microscope equipped with TTL. For the lowest light power setting (DLD), 0.0911 mW of incident light power was delivered to the sample over a 15,909 ms exposure time. This power corresponded to a final intensity of 0.03% from the light source [3% power, 1% neutral density (ND) filter (optical density (OD)=2)]. For the highest light power setting (CLD), 61.6 mW of incident light power was delivered over a 24 ms exposure time. Regardless of the light power, the amount of paxillin–EGFP signal remaining after 300 frames was not statistically different between imaging conditions that ranged from DLD to CLD when TTL was employed (Fig. 2A). This demonstrates that the total number of photons impacting the sample determines the degree of photobleaching, rather than how light is delivered. To further characterize the photobleaching, fixed cells expressing paxillin–EGFP were imaged in the presence of CellROX™, a fluorogenic probe used for measuring cellular oxidative stress. Exposure time did not affect the amount of ROS produced when the number of photons between conditions was kept constant (Fig. 2B); however,

Journal of Cell Science (2020) 133, jcs242834. doi:10.1242/jcs.242834

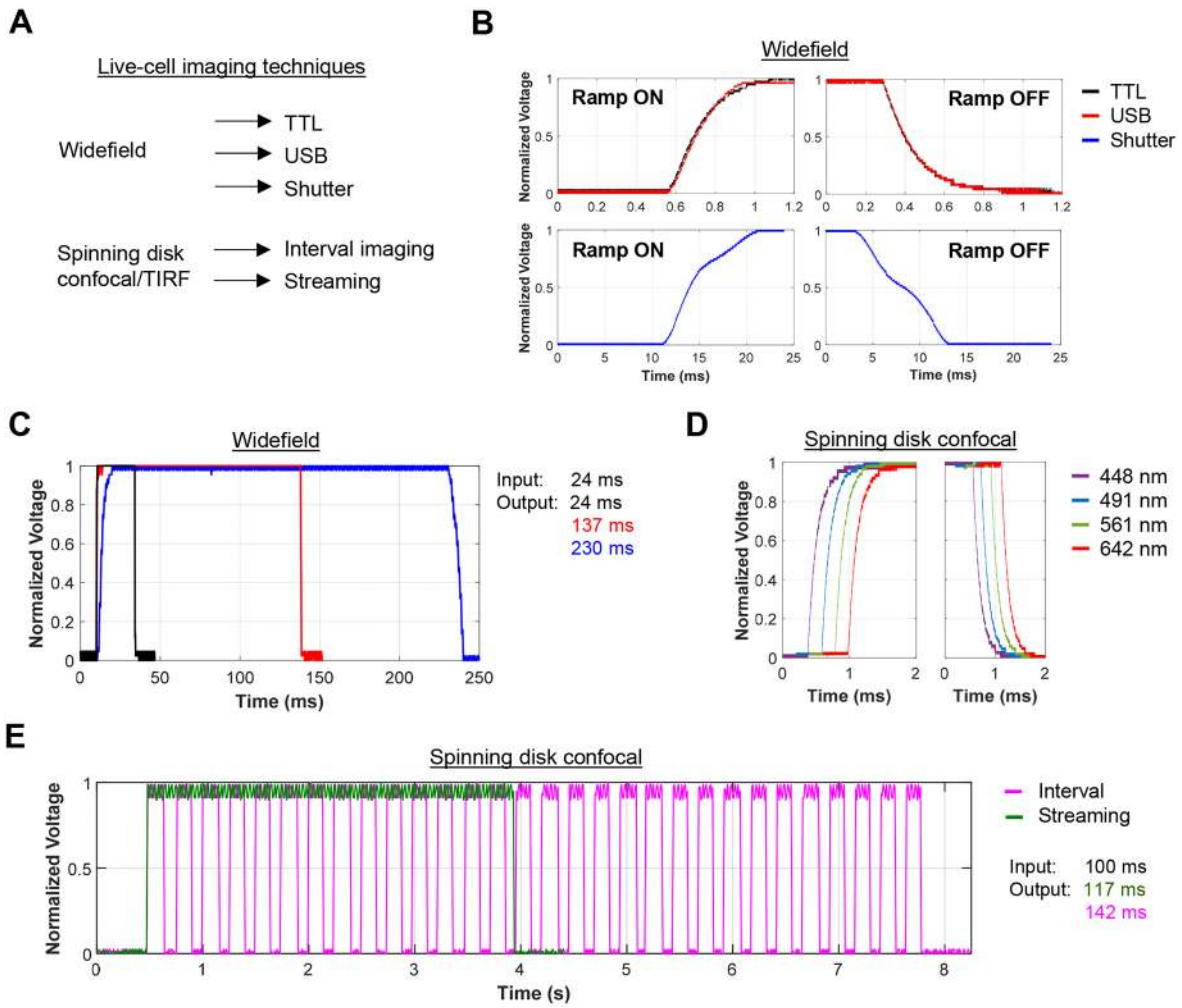

Fig. 1. Standard imaging protocols deliver additional sample illumination beyond input camera exposure time. (A) Microscopy techniques commonly used for live-cell imaging. Mechanical shutters were traditionally used for sample illumination. Modern LED light sources (widefield microscopy) can be activated through the microscope software using a USB connection or by a transistor-transistor logic (TTL) circuit between the camera and light source. Solid-state lasers (spinning disk confocal microscopy) deliver sample illumination using an acousto-optic tunable filter (AOTF) crystal that is controlled by the microscope software through a USB connection. Interval imaging allows users to set a time delay between subsequent image acquisitions. Stream acquisition allows users to capture images as quickly as possible (up to the camera frame rate) with the sample constantly illuminated. (B) Ramp on/off times were measured on a widefield microscope using a mechanical shutter, USB or TTL light source activation. (C) Total illumination time delivered by the shutter, USB or TTL for an input camera exposure time of 24 ms. (D) Ramp on/off times were measured on the SD confocal microscope using electronic activation (through the AOTF crystal). (E) Total illumination time delivered by interval or stream acquisition on the spinning disk confocal microscope. Camera exposure time was set to 100 ms. A total of 30 frames were captured with the imaging interval set to 0 ms.

if the light power was increased, the amount of ROS production was directly related to the total light dose (Fig. 2C).

Phototoxicity is often measured by quantifying cell division or cell death after live-cell experiments (Douthwright and Sluder, 2017; Laissue et al., 2017; Wäldchen et al., 2015). These assays can measure the impact of phototoxicity but they take a long time to conduct and more subtle phototoxic effects may go unnoticed. Our previous experience shows that cell migration rates are sensitive to phototoxicity (Knoll et al., 2015; Mubaid and Brown, 2017). Therefore, the migration speeds of CHO-K1 cells expressing paxillin–EGFP were assessed in response to different illumination conditions (Table S2). Cell migration speeds from fluorescence images generated with CLD (61.6 mW×24 ms) were similar to those measured with DLD (0.245 mW×60,000 ms) (Fig. 2D,E). Importantly, the migration rates measured from both sets of fluorescence images were not significantly different than those measured from brightfield images (Fig. 2D,E). A camera exposure time of 60,000 ms was chosen to fill the delay time of 1 min between images (continuous illumination). The 0.0245 mW of power used corresponded to a power density (i.e. irradiance) of 1.52 mW cm^{-2} (Table S2) or 0.007% light source intensity, which is significantly lower than that used by most researchers for live-cell experiments [7% lamp intensity, 10% ND filter (OD=1) and 1% ND filter (OD=2)]. Given that ROS production is dependent on total light dose rather than exposure time, cell migration experiments were subsequently repeated with an increased frequency of TTL pulses (Fig. 2F) or incident light power (Fig. 2G; Table S3). Increasing the imaging frequency of CLD had a similar effect on cell migration speeds when compared to increasing the light power of DLD. Cell migration speeds remained unaffected up to a 3-fold increase in total light dose but were significantly reduced with further increases in light power (Fig. 2H,I). Thus, total light dose, rather than exposure time, is the main determinant of ROS production and cell health. As a result, it is best to implement TTL light triggering if possible.

Journal of Cell Science (2020) 133, jcs242834. doi:10.1242/jcs.242834

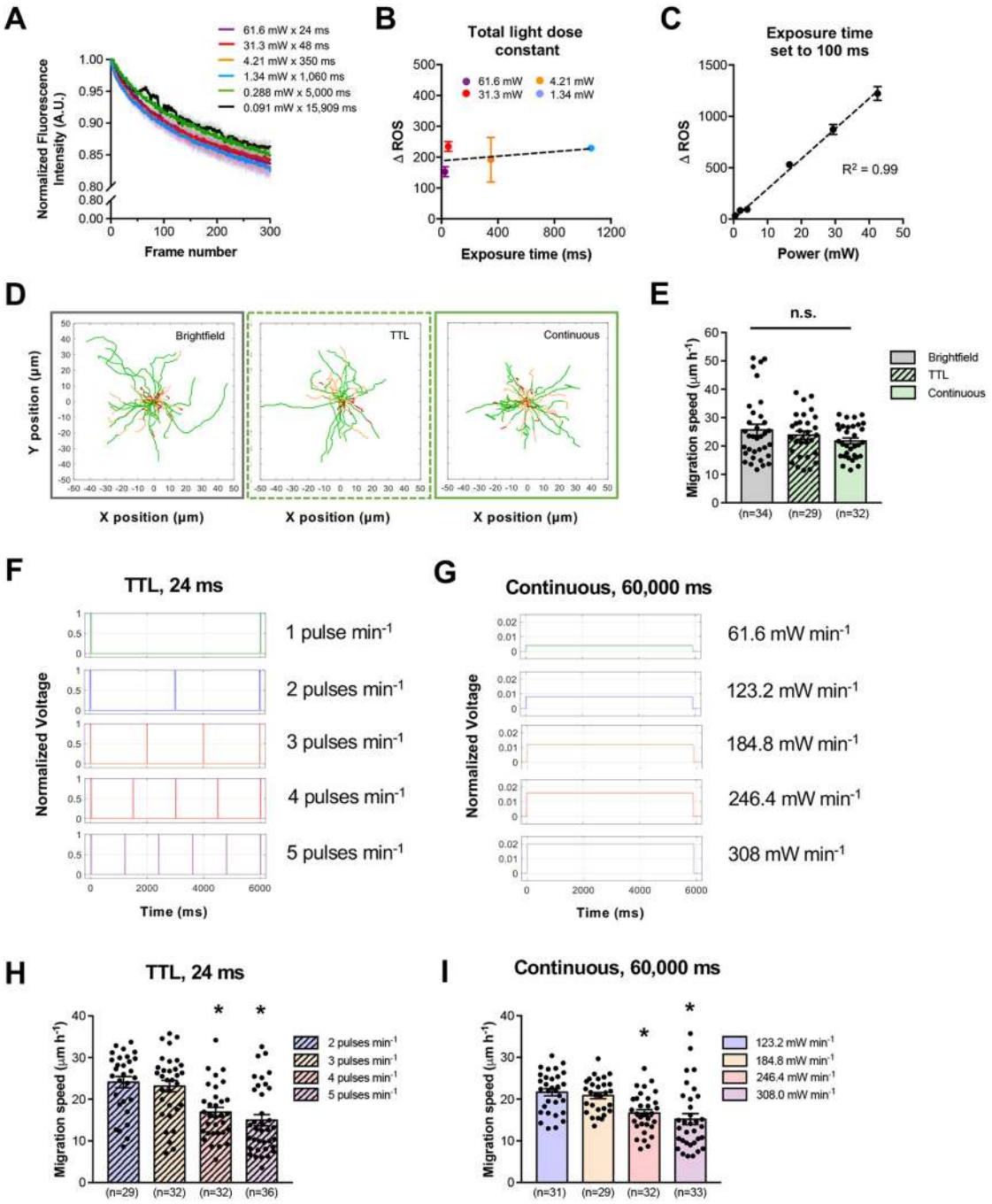

Fig. 2. Total light dose and ROS are tightly linked processes that cause phototoxicity. (A) CHO-K1 cells stably expressing paxillin–EGFP were fixed with 4% PFA and repeatedly imaged with a 20×0.8 NA objective lens on a widefield microscope equipped with TTL. Photobleaching decay curves were normalized to the maximum fluorescence intensity of each experiment. Data represents the average of three independent experiments. Shaded areas represent mean±s.e.m. (B) Paxillin–EGFP was photobleached with different light power regiments in the presence of CellROX™. Data represent the mean±s.e.m. of three independent experiments. (C) Paxillin–EGFP was photobleached with increasing light power, and ROS production was imaged through the addition of CellROX™. Camera exposure time was set to 100 ms. Data represent the mean±s.e.m. of three independent experiments. (D) CHO-K1 cell migration tracks in the presence of brightfield (n=34), TTL (61.6 mW×24 ms) (n=29) or continuous (0.0245 mW×60,000 ms) (n=32) illumination. Each line presents the path of a single migrating cell over 1.5 h. Tracks are color-coded based on cell speed calculated for every 10-min interval: <15 μm h^{-1} (red), 15–25 μm h^{-1} (orange), >25 μm h^{-1} (green). (E) Migration speed (mean±s.e.m.) of cells in each condition depicted in D. (F,G) Imaging frequency for TTL, and incident light power for continuous imaging, was increased 2-, 3-, 4- and 5-fold, respectively. (H) Migration speed (mean±s.e.m.) of cells captured with the imaging frequencies described in F. Number of cells analyzed is indicated in parentheses. *P<0.001 from 1 pulse min^{-1} (two-tailed Student's t-test). (I) Migration speed (mean±s.e.m.) of cells captured with the different light powers described in G. Number of cells analyzed is indicated in parentheses. *P<0.001 from 0.245 mW min^{-1} (two-tailed Student's t-test).

Journal of Cell Science (2020) 133, jcs242834. doi:10.1242/jcs.242834

Longer exposure times reduce the impact of IO and improve cell health

Although TTL triggering of LED and solid-state light sources has been in use for over a decade, TTL is not yet a standard feature on most microscopy platforms. Moreover, these microscope configurations are not well known in the biological imaging community and implementation of TTL circuits may require an override of the microscope software control. Given the measurements showing that USB lamp control and mechanical shutters result in substantially longer exposure times than the desired input (Fig. 1C), the relative impact of IO with different imaging conditions was measured.

Similar to the experiments shown in Fig. 2, camera exposure times were scaled with illumination power to maintain a constant number of photons during image acquisition but without accounting for the contribution from IO (Table S2). In our experience, this is how most microscope users configure a live-cell imaging experiment. USB triggering was used to control the LED light source as installed and configured by the manufacturer. Strikingly, IO had the largest impact with short exposure times; in particular, the percentage contribution of IO was ∼470% for an input camera exposure time of 24 ms (CLD) (Fig. 3A; Fig. 1C). In contrast, the percentage contribution for 60,000 ms (DLD) was only 0.67% (Fig. 3A; Fig. S1D). As a result, increasing the exposure time significantly reduced the amount of photobleaching experienced by CHO-K1 cells expressing paxillin–EGFP (Fig. 3B) and exponentially decreased the amount of ROS produced (Fig. 3C). This is because the relative contribution of IO was reduced at lower powers when longer exposure times were used (Fig. S1A–D). The CHO-K1 cell migration assay was used to test the impact of IO on cell health. Longer exposure times with lower light powers (DLD), resulted in significantly faster cell migration speeds than short exposure, high light power conditions (CLD) (Fig. 3D,E; Movie 1). In particular, cell migration speeds measured from fluorescence images captured with exposure times greater than 1060 ms were similar to those measured with brightfield imaging (Fig. 2E).

Changes in mitochondrial morphology are thought to occur early in the apoptotic process (Karbowski and Youle, 2003). Studies indicate that excessive ROS production causes the release of cytochrome *c* and other pro-apoptotic proteins, which results in mitochondrial remodeling and fragmentation (Ott et al., 2002). Thus, mitochondrial morphology was assessed as an additional sensitive readout of cell health. Live cells were stained with MitoTracker™ Red and immediately fixed with PFA. Cells exposed to CLD (61.6 mW×24 ms) exhibited condensed/fragmented mitochondrial networks in the perinuclear region (Fig. 3F), similar to the positive controls (cells treated with H_2O_2, a ROS inducer; Willems et al., 2015) (Fig. 3F). In contrast, mitochondrial morphology was maintained following DLD (0.0245 mW×60,000 ms) even after 16 h of continuous illumination (Fig. 3F; Movie 2). To verify that changes in mitochondrial morphology were the direct result of light exposure, mitochondria were imaged in live cells over time using a high resolution 63×1.4 NA oil objective lens (Table S4). Cells illuminated with DLD (0.0093 mW×60,000 ms) had a healthy mitochondrial network even after 4 h of continuous light exposure (Fig. 3G; Movie 3). In contrast, CLD (21.3 mW×24 ms) led to a retracted and fragmented mitochondrial network (Fig. 3H; Movie 3) due to excess light from IO. Measurements of cell and mitochondrial morphology indicated that cells were rapidly affected by CLD (Fig. 3I,J).

To determine the general applicability to other biological systems and fluorescent probes, the cell migration assay was conducted on normal murine mammary gland (NMuMG)-ErbB2 cells derived from mouse tumor explants (118; Northey et al., 2008; and 87, Northey et al., 2013) and 4T1 cells derived from liver metastases (Tabariès et al., 2011) (Table S5). NMuMG-ErbB2 cells expressing LifeAct tagged with blue fluorescent protein (BFP-LifeAct) showed dramatically reduced speeds under CLD (34 mW×24 ms), but not DLD (0.015 mW×60,000 ms) (Fig. S1E). Similarly, 4T1 cells expressing the cell matrix adhesion protein lipoma preferred partner (LPP) fused to mCherry, were significantly affected by CLD (58 mW×100 ms), but not DLD (0.099 mW×60,000 ms) (Fig. S1F). Finally, cell migration speeds of NMuMG-ErbB2 cells expressing the adapter protein ShcA (also known as SHC1) tagged with a far-red fluorescent protein, miRFP670 (Shcherbakova et al., 2016), were significantly affected by CLD (63 mW×100 ms), but not DLD (0.110 mW×60,000 ms) (Fig. S1G). These results demonstrate that DLD is a simple and generalized method to minimize photobleaching and phototoxicity when TTL triggering of the light source is not possible.

Images collected with DLD conditions are of high quality

Charge-coupled device (CCD) cameras are commonly used to acquire fluorescence microscopy images. CCD cameras are primarily affected by shot noise and dark noise. Shot noise results from the inherent variation in the arrival rate of photons at the camera. Because it is dependent on the signal level measured, shot noise is insignificant when the signal is sufficiently large (Murray, 1998). In contrast, dark noise arises from a random number and location of electrons thermally generated within the sensor (Salmon and Waters, 2011). Dark noise is essentially negligible with short exposure times because of camera cooling; however, long exposure times can cause significant buildup on the camera (Spring, 2007). Read noise is also important but it is not dependent on exposure time.

To explore the impact of noise on the quality of images, fixed cells expressing paxillin–EGFP were imaged with a 20×0.8 NA objective lens and 12 different illumination settings (Table S6). The intensity of paxillin–EGFP was similar between illumination conditions as the number of photons applied to the sample was kept constant; however, the standard deviation of the background increased linearly with exposure time (Fig. S2A–F). Consequently, images captured with exposure times greater than 23 s had significantly lower signal-to-noise ratios (S/N) than images captured with 24 ms exposure time (Fig. S2D). Importantly, S/N was not significantly different for exposure times between 1 and 23 s, which were found to be conducive to good cell health.

In general, images captured with DLD conditions retained reasonable S/N; however, S/N could be substantially improved by slightly increasing the excitation light power (Fig. S2G,H; Table S7). A 3-fold increase still maintained a low light power (0.070 mW×60,000 ms) and surpassed the S/N of images captured with CLD (61.6 mW×24 ms). Importantly, a 3-fold increase in power did not cause a significant reduction in cell migration speeds (Fig. 2I). Collectively, these results demonstrate that DLD conditions can be used to generate high-quality images that are comparable to those captured with CLD conditions.

Imaging of dynamic processes is severely impacted by IO

IO can significantly impact image quality and photobleaching of fluorescent dyes (Fig. 3B). More importantly, it can lead to additional phototoxic effects on the sample (Fig. 3D–H). Therefore, the impact of IO on dynamic processes, which require shorter exposure times and higher resolution objective lenses, was explored on the SD microscope.

Journal of Cell Science (2020) 133, jcs242834. doi:10.1242/jcs.242834

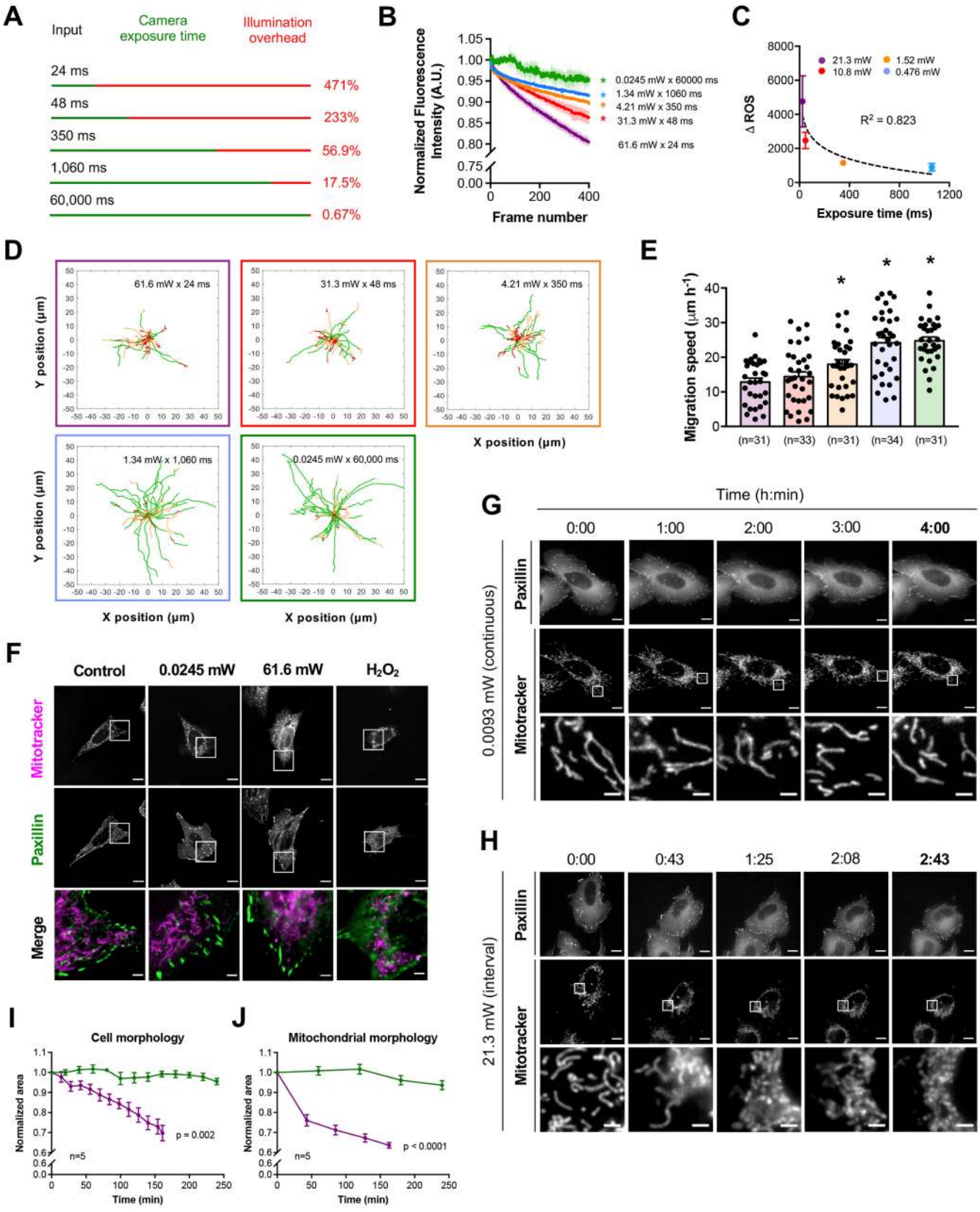

Fig. 3. See next page for legend.

LLC-PK1 cells stably expressing the microtubule-associated protein EB3, fused to mEmerald (EB3–mEmerald), were imaged with a 63×1.40 NA oil objective lens. EB3 transiently binds to the tip of growing microtubules, which develop at a speed of at least 0.5 μm s^{-1} (Komarova et al., 2009; Stepanova et al., 2003). Accordingly, an sCMOS camera capable of acquiring high resolution images

Fig. 3. Longer exposure times reduce the impact of IO. (A) Percentage contribution of IO for different input camera exposure times when using a USB for light source activation (AOTF crystal). (B) Photobleaching decay curves of CHO-K1 cells expressing paxillin–EGFP in response to different light power regiments. Images were acquired with 20×0.8 NA objective lens on a widefield microscope. Curves were normalized to the maximum fluorescence intensity of each experiment. Data represents the average of three independent experiments. Shaded areas represent mean±s.e.m. (P<0.04 from 61.6 mW×24 ms, two-tailed Student's t-test for area under the curve). (C) Paxillin–EGFP was photobleached with different light power regiments in the presence of CellROX™. Data represent the mean±s.e.m. of three independent experiments. (D) Live-cell migration tracks of CHO-K1 cells expressing paxillin–EGFP in response to different light power regiments (n=31 for 61.6 mW×24 ms; n=33 for 31.3 mW×48 ms; n=31 for 4.21 mW×350 ms; n=34 for 1.34 mW×1060 ms; n=31 for 0.0245 mW×60,000 ms). Each line presents the path of a single migrating cell over 1.5 h. Tracks are color-coded based on cell speed calculated for every 10-min interval: <15 µm h^{-1} (red), 15-25 µm h^{-1} (orange), >25 µm h^{-1} (green). (E) Migration speed (mean±s.e.m.) of each cell depicted in D. Number of cells analyzed is indicated in parentheses. *P<0.005 from 61.6 mW×24 ms (two-tailed Student's t-test). (F) Migrating cells were stained with MitoTracker™ Red and fixed with 4% PFA to visualize mitochondrial morphology. Cells were exposed to no light (control), 0.0245 mW of light power continuously for 16 h, 61.6 mW of light power intermittently (24 ms) for 3 h, or 250 µM of H_2O_2 (no light exposure) for 3 h. Scale bars: 10 µm for whole-cell images and 2 µm for magnified images. (G,H) CHO-K1 cells were stained with MitoTracker™ Red and imaged with DLD (0.0093 mW×60,000 ms) or CLD (21.3 mW×24 ms) using a 63×1.4 NA oil objective. Images for paxillin–EGFP and MitoTracker™ Red were acquired every minute and 6 min, respectively. Scale bars: 10 µm for whole-cell images and 2 µm for magnified images. (I,J) Changes in cell area and mitochondrial area over time (n=5 cells from three independent experiments). Measurements were normalized to initial cell area at time zero. Results represent mean±s.e.m. (P-values correspond to Student's t-test for area under the curve).

(0.0586 µm $pixel^{-1}$) with fast frame rates (10 ms) was used to capture this dynamic process. Images were captured with stream acquisition, as this method eliminates the need for repeated triggering of the light source and synchronization with the camera. Thus, the only major contributing factor to IO was the read speed of the camera and time for the computer to save the digital image. IO was measured to be 17 ms (Fig. 1E). Consequently, with shorter exposure times, IO comprised a significantly greater proportion of overall light exposure. For example, with the camera exposure time set to 10 ms, IO comprised ∼170% of the total illumination time (Fig. 4A). In contrast, IO led to an additional ∼8% of light exposure when the camera exposure time was set to 217 ms (Fig. 4A). The impact of different exposure times on S/N was explored. Given the fact that IO contributes to phototoxicity, light power was adjusted to compensate for IO so that the same total light dose was delivered for each imaging condition (Table S8). The S/N of EB3 dramatically improved with increasing exposure time as the percentage contribution of IO decreased (Fig. 4B,C). To collect images with a comparable S/N, light power needed to be increased for shorter exposure times (Fig. S3). These higher light powers caused rapid photobleaching after just 2 min (Fig. 4D). Indeed, only 26% of mEmerald signal remained after 2 min of CLD (0.922 mW), while DLD (0.0167 mW) resulted in little photobleaching (Fig. 4D). Thus, IO is especially detrimental when imaging dynamic processes with short exposure times under CLD conditions.

Systematic determination of maximum image exposure time for dynamic processes

Longer camera exposure times can be used to improve image S/N and reduce photobleaching and phototoxicity caused by IO. Unfortunately, longer exposure times can also cause object blurring when capturing dynamic processes. As a result, a workflow was developed to systematically determine the longest exposure time possible to generate high S/N images but avoid image blur from rapidly moving structures. Dynamic EB3–mEmerald structures were used to demonstrate the workflow.

First, temporal image stacks of EB3–mEmerald were acquired with a 10 ms exposure time. Maximum intensity projections of several frames were then generated to mimic longer exposure times (Fig. 4E). Camera exposure times appropriate for measuring cell migration resulted in significant motion blur of EB3 (Fig. 4E). To objectively determine the maximum exposure time without significant image blur, image analysis software was used to determine the area, roundness and length of EB3 spots localized to microtubule tips in the maximum projection images that mimicked different exposure times (Fig. 4F–H). Based on these parameters, it was clear that microtubule dynamics should be imaged with an exposure time no longer than ∼500 ms (Fig. 4F–H). Longer exposure times caused significant blur and distorted the size and shape of EB3 structures, such that images were no longer representative of accurate EB3 localization.

Imaging two fluorescent probes in the same live sample has a higher chance of causing phototoxicity, and dual infection or transfection of fluorescent proteins can make cells more sensitive to external stressors (Fiszer-Kierzkowska et al., 2011). The LLC-PK1 cells were engineered to co-express EB3–mEmerald and the histone-binding protein H2B–mCherry. Therefore, dual-color live-cell imaging of both probes was performed. Given the fact that mEmerald is a relatively unstable fluorophore (Shaner et al., 2005), light levels were reduced to the lowest possible level while maintaining sufficient S/N for EB3 microtubule tip-tracking analysis. With a modest exposure time of 200 ms (<500 ms maximum exposure determined above), images of EB3–mEmerald (491 nm; 0.020 mW) and H2B–mCherry (561 nm; 0.010 mW) were collected simultaneously with a beam splitter and two sCMOS cameras (Fig. 4I; Movie 4). Importantly, these laser powers caused minimal photobleaching on fixed samples (Fig. 4J).

Image processing can be used to improve S/N of images and subsequent image analysis

Image processing techniques can be used to enhance S/N as an alternative to increasing total light dose. First, temporal image stacks of EB3–mEmerald were summed to simulate images taken with longer exposure times (Fig. S4A). A 2×2 median filter was then applied to the images to remove spurious noise (Fig. S4C). For each exposure time tested, there was approximately a 4-fold increase in S/N due to increased signal and reduced noise (Fig. S4B,D). Filtering did significantly reduce mean intensity at most exposure times (likely due to the removal of high intensity noise pixels) but did not affect EB3 morphology (area, roundness and length) (Fig. S4E–H). Finally, a 2×2 median filter was applied to dual-color EB3 time-lapse data described in Fig. 4I. Filtering improved object detection and tracking by removing spurious noise (Fig. S4I). As a result, measurements of area, roundness and length were determined more precisely from filtered images (Fig. S4J). Importantly, the mean and standard deviation of EB3 speed was found to be identical between raw and filtered data, and in line with previously published results (Komarova et al., 2009; Stepanova et al., 2003).

Spatial and temporal binning are two other image processing techniques that may be used to improve the S/N of images. To demonstrate the benefit of binning, lysosomal structures in CHO-K1 cells stained with LysoTracker™ Green were imaged on the SD microscope (Table S9). Note that spatial binning on sCMOS

Journal of Cell Science (2020) 133, jcs242834. doi:10.1242/jcs.242834

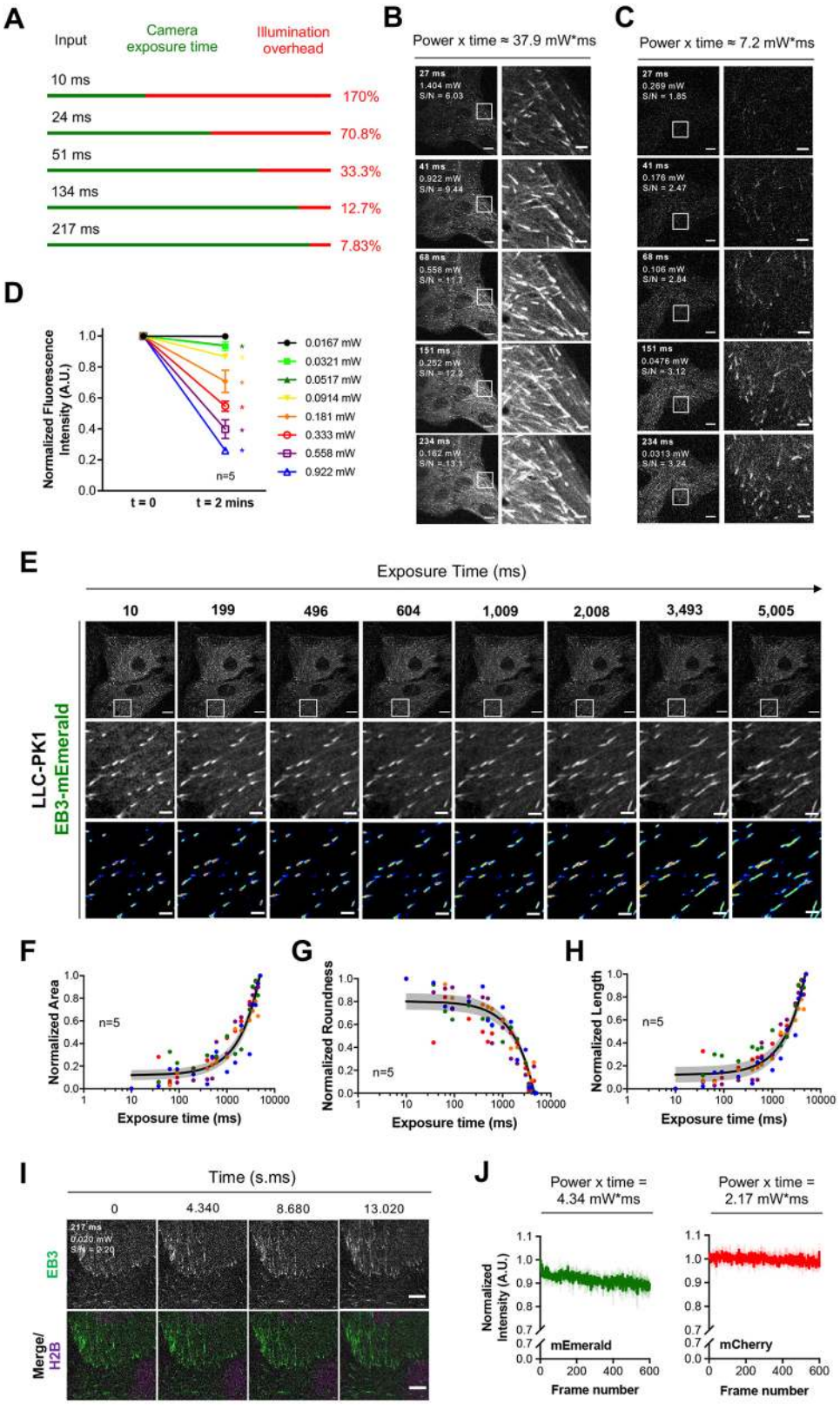

Fig. 4. Object shape can be used to determine the longest exposure time for a dynamic process. (A) Percentage contribution of IO for several exposure times. IO was found to be 17 ms for stream to RAM image acquisition on the spinning disk confocal microscope. (B,C) Representative images of LLC-PK1 cells stably expressing EB3–mEmerald and H2B–mCherry showing the effect of IO on the S/N. Images were acquired with a 63×1.40 NA oil immersion objective lens. Scale bars: 10 µm for whole-cell images and 2 µm for magnified images. (D) Photobleaching decay curves of EB3–mEmerald in live LLC-PK1 cells (mean± s.e.m.; n=5 from three independent experiments). *P<0.05 from 0.0167 mW (two-tailed Student's t-test). (E) LLC-PK1 cells were rapidly imaged on a spinning disk confocal microscope with a 63×1.40 NA oil objective. Maximum intensity projections were generated from 10 ms frames to simulate data captured with different exposure times. Scale bars: 10 µm for whole-cell images and 2 µm for magnified images. (F–H) Area, roundness and length of EB3 signal localized to microtubule tips were determined from images in E. Values were normalized to a scale of 0–1. Individual data points are color-coded by cell (n=5). Shaded areas represent mean±s.e.m. (I) Dual-color imaging of EB3–mEmerald and H2B–mCherry. Camera exposure time was set to 200 ms based on EB3 morphology measurements. Scale bar: 5 µm. (J) Photobleaching decay curves of mEmerald and mCherry from fixed LLC-PK1 cells. Curves were normalized to the maximum fluorescence intensity of each experiment. Data represents the average of three independent experiments. Shaded area represents mean±s.e.m.

cameras is performed post image acquisition and does not provide as much benefit in speed as with CCD cameras. Thus, spatial binning can simply be performed as a post image acquisition processing step. Previous studies have shown that lysosomes move at ∼0.38 µm s^{-1} (Valm et al., 2017). Accordingly, a 100 ms exposure time was fast enough to image lysosomes using a 63×1.40 NA oil immersion objective lens without any evidence of motion blur (Fig. 5A, top left image). Moreover, images collected with 100 ms exposure time had sufficient S/N for automated tracking (data not shown). Spatial pixel binning (post image acquisition

Journal of Cell Science (2020) 133, jcs242834. doi:10.1242/jcs.242834

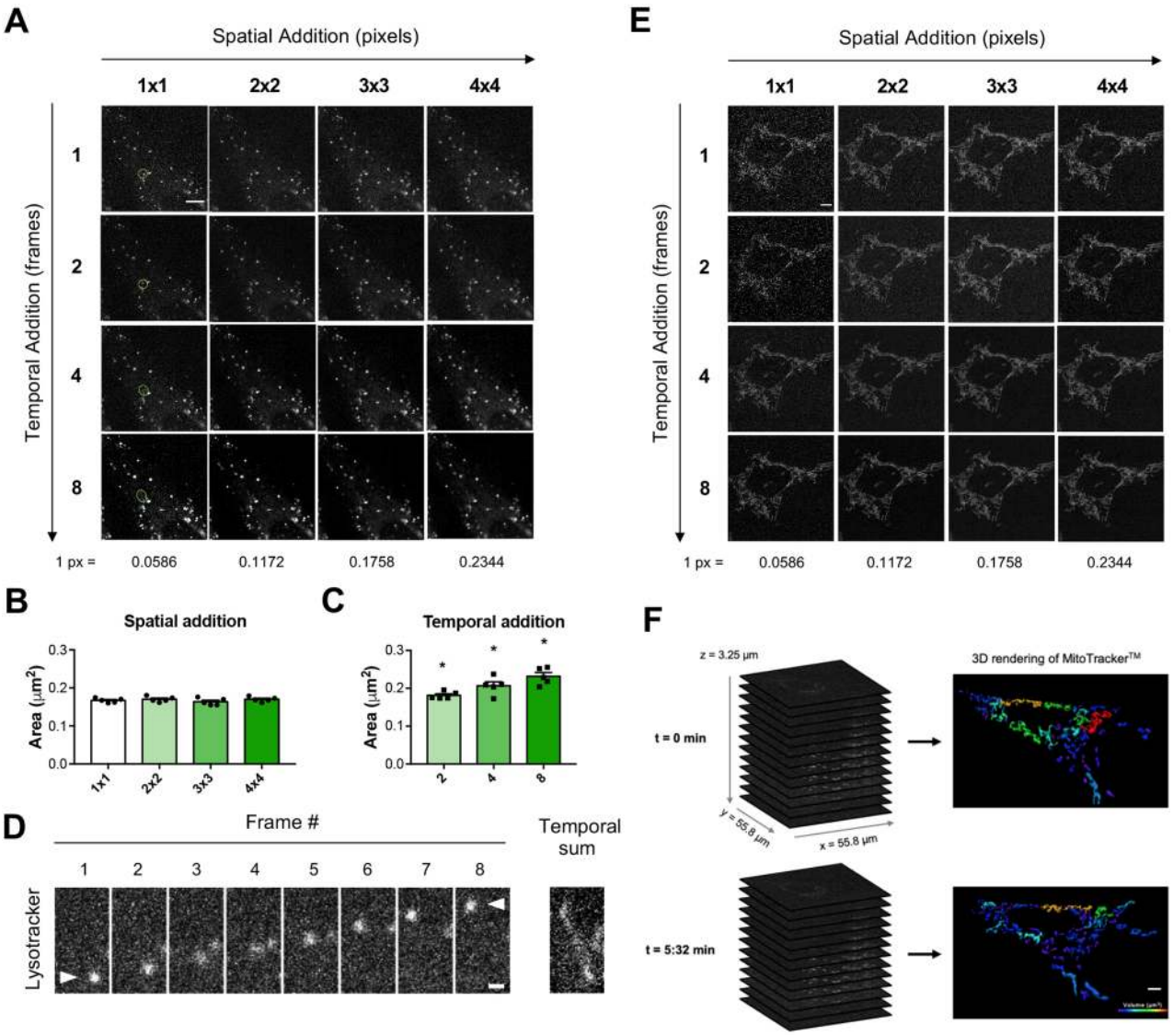

Fig. 5. Spatial and temporal binning can be used to improve S/N of images. (A) CHO-K1 cells stained with Lysotracker™ Green were imaged on an SD microscope with a 63×1.40 NA oil objective. Camera exposure time was set to 100 ms. Spatial addition was achieved by adding pixels together; temporal addition was achieved by adding images together. Brightness and contrast were adjusted for each image to highlight any changes in morphology. Scale bar: 5 µm. (B,C) Analysis of lysosomal morphology following spatial and temporal addition. Black dots indicate the average for each cell analyzed (n=5). Bars represent mean±s.e.m. *P<0.05 from 1×1 binning (Mann–Whitney U-test). (D) High-magnification montage of green oval in A showing the eight image frames that were added together. The white arrowhead points to a rapidly moving lysosome that caused streaking in the temporally binned image. Scale bar: 0.7 µm. (E) CHO-K1 cells stained with MitoTracker™ Red were imaged with a camera exposure time of 100 ms. Spatial and temporal addition were performed as described for A. Brightness and contrast were adjusted for each image to highlight any changes in morphology. Scale bar: 5 µm. (F) Three-dimensional time-lapse of mitochondrial dynamics. A 13-slice z-stack with a step size of 0.25 µm was continuously acquired for 5.5 min. Surfaces were statistically coded based on volume. Camera exposure time was set to 50 ms with 2×2 binning. Scale bar: 4 µm.

processing) of high-resolution sCMOS images could be used to improve S/N (Fig. 5A, moving across rows). This method of image processing greatly increased the signal for each lysosomal structure (Fig. S5A) without significantly affecting lysosomal area (Fig. 5B). Temporal addition of successive image frames could also be used to improve S/N (Fig. 5A, moving down columns; Fig. S5B). There was a limit, however, as temporal addition of eight images resulted in significant motion blur of fast-moving lysosomes (Fig. 5C,D). Therefore, spatial pixel addition would be the preferred method of increasing S/N if objects are moving rapidly and temporal resolution must be maintained.

Spatial and temporal pixel binning were then investigated as tools for measuring mitochondrial dynamics. CHO-K1 cells were stained with MitoTracker™ Red and imaged with a 63×1.40 NA oil objective (Table S9). In line with the lysosomal data, spatial addition generated images with higher S/N without significantly impacting mitochondrial morphology (Fig. 5E). Mitochondria are much less dynamic than lysosomes (Twig et al., 2008). As a result, temporal binning of 100 ms images could also be used to improve S/N without introducing any obvious spatial blur (Fig. 5E). Combining both spatial binning of 4×4 pixels and temporal addition of eight sequential time-lapse image frames tremendously increased the signal captured for MitoTracker™ Red (Fig. S5C). Therefore, conditions to capture a three-dimensional video of mitochondrial dynamics were explored. Images could be acquired continuously with a z-stack of 15 images for ∼5 min without any evidence of

Journal of Cell Science (2020) 133, jcs242834. doi:10.1242/jcs.242834

phototoxicity (Movie 5). After spatially binning images (2×2) and removing spurious noise with a median filter (2×2), the volume of the mitochondrial networks was determined over time with a pixel resolution of 0.1172 µm in *x*,*y* and 0.25 µm in *z* with no evidence of motion blur (Fig. 5F).

DLD can be used to reveal and measure fast adhesion dynamics

Having explored the relationship between exposure time and cell health, continuous imaging of cell matrix adhesion dynamics with high temporal resolution was explored. Nascent adhesions found at the protruding edge of the cell are typically sub-resolution (<1 µm in diameter) and have a short lifespan (<1 min) (Choi et al., 2008; Zaidel-Bar et al., 2003). Traditionally, however, adhesion dynamics have been measured with a temporal resolution of 15–30 s (Berginski et al., 2011; Delorme-Walker et al., 2011; Nayal et al., 2006). With this knowledge in mind, camera exposure time on the SD microscope was set to 5 s. 4T1-derived lung-metastatic breast cancer cells (4T1-537; Rose et al., 2010) were then transfected with mCherry–paxillin and continuously imaged with DLD conditions for 20 min using a 63×1.40 NA oil immersion objective (Fig. 6A; Table S9). This resulted in high S/N images with superior temporal resolution for measuring adhesion dynamics and minimal contributions from IO (Movie 6). High S/N images and improved temporal resolution achieved with continuous imaging improved the ability of automated tracking algorithms to accurately segment adhesions and determine slow and intermediate adhesion assembly and disassembly rates [Fig. 6B, red (slow), orange (intermediate) traces]. Furthermore, rapid adhesion dynamics that were not detected with previous image acquisition settings were easily visualized and quantified (Fig. 6B, green traces). In contrast, measuring adhesion dynamics with a time delay of 20–30 s between images resulted in a significant loss of information (Fig. 6C), which contributed to a lower accuracy in determining adhesion assembly and disassembly rates (Fig. 6D–F). These experiments were repeated with CHO-K1 cells expressing paxillin–EGFP (Fig. S6; Table S9). A 20 s time resolution also resulted in a significant underestimation of adhesion assembly and disassembly rates in these cells (Fig. S6).

Given the success in capturing fast adhesion dynamics, DLD was explored for the simultaneous capture of adhesion and actin dynamics in migrating cells. Using continuous imaging, rapid actin cytoskeleton dynamics were captured in parental NMuMG cells stably expressing LifeAct–EGFP with no evidence of photobleaching or phototoxicity (Movie 7; Table S9). CHO-K1 cells expressing paxillin–EGFP were then transfected with LifeAct–mRuby and continuously imaged with a 5 s time resolution (Table S9). Dual-color imaging of the actin cytoskeleton and adhesions was performed with little photobleaching and no evidence of phototoxicity (Movie 8).

Finally, DLD was used to image NMuMG-ErbB2 cells stably expressing a vinculin tension sensor, which contains the relatively unstable teal (TFP) and venus fluorescent proteins (Grashoff et al., 2010). High S/N images with minimal phototoxicity were obtained using a 63×1.40 NA oil immersion objective. TFP was excited with 0.013 mW from a 448 nm laser over a period of 20 min and venus fluorescent protein was excited with 0.007 mW from a 491 nm laser for an additional 20 min (Fig. 6G; Table S9). Dynamic adhesions were observed with a camera exposure time of 5 s despite the reduced photostability of these proteins compared to EGFP (Shaner et al., 2005). In fact, photobleaching of these proteins in fixed samples was minimal with continuous DLD imaging conditions (Fig. 6H).

In general, the results presented here show that the entire time delay between images can be harnessed to collect light from low-power fluorescence excitation. DLD allows researchers to capture more information about biological processes without artifacts from cell damage. On the other hand, more rapid biological events may not be observed if shorter exposure times with higher light levels and longer delays between successive images (CLD) are used on microscopes without TTL.

DISCUSSION

In the present study, we show that photobleaching and ROS production are tightly linked processes that lead to phototoxicity. Conventional live-cell imaging protocols recommend the use of short exposure times with higher light powers (CLD) (Carlton et al., 2010; Frigault et al., 2009; Swedlow et al., 2009; Wäldchen et al., 2015). On the other hand, several studies cite the benefit of longer exposure times with lower light powers (DLD) (Icha et al., 2017). Proponents of the latter approach argue that DLD alleviates pressure on cellular mechanisms designed to eliminate ROS. This study shows that CLD and DLD produce similar levels of ROS. Instead, much of the phototoxicity caused by high power fluorescence illumination can be attributed to additional light exposure beyond the camera exposure time (i.e. IO). If microscopes are not configured with a TTL trigger, such that the sample is only exposed to light during the acquisition time, then phototoxicity caused by IO is much more of an issue with CLD than DLD. Opening and closing of physical shutters, electronic switching of light sources, ramp up/down times for the light source to reach peak power and delays in camera software drivers can all impact IO. Software control that leaves the light source enabled during image read time, analog-to-digital conversion, and image write time to the computer memory or hard drive can further impact IO. In some cases, IO can be effectively eliminated by installing a TTL circuit between the camera and light source. By allowing the camera to control light source activation, microscope software does not need to synchronize camera acquisition, illumination and data saving.

Unfortunately, TTL implementation is not always possible, such as with bulb-based widefield microscopes and the SD confocal microscope used in this study. These types of light sources and microscopes are broadly used in the bioimaging community. Measuring actual light delivery during microscopy imaging may also be technically challenging. As a general solution, this work shows that researchers can implement longer exposure times (DLD) on microscopy platforms without the need for TTL. DLD can generate high S/N images and does not require the addition of chemicals to living samples, such as reducing agents or ROS scavengers, which may alter the physiological properties under study (Alejo et al., 2013; Knight et al., 2003; Wäldchen et al., 2015). In addition, it does not require the removal of nutrients that may be required by living samples (Bogdanov et al., 2009, 2012). DLD can be broadly applied to image blue, cyan, green, yellow, red and far-red fluorescent proteins and dyes with minimal photodamage to live cells. DLD also does not restrict live-cell imaging to slow biological processes. Stream acquisition or continuous illumination with longer exposure times can be used to measure rapid cellular processes, on the scale of milliseconds, such as lysosomal, mitochondrial and microtubule tip dynamics. By acquiring fluorescence emission during the entire time delay between image frames, sufficient temporal resolution and S/N can be obtained for fast dynamics and three-dimensional time-lapse movies. Furthermore, DLD can enable more frequent capture of fluorescence images because the percentage contribution of IO

Journal of Cell Science (2020) 133, jcs242834. doi:10.1242/jcs.242834

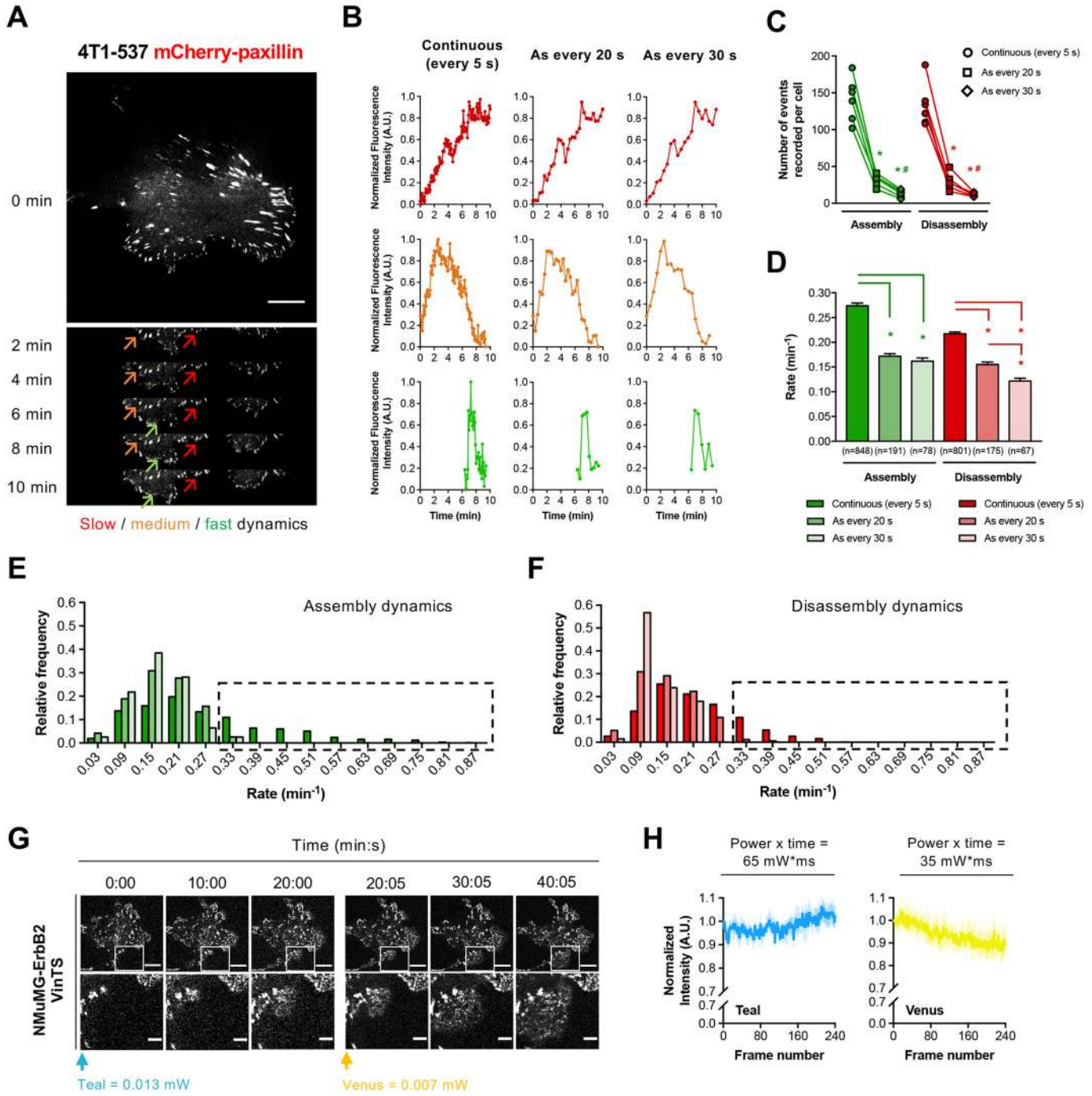

Fig. 6. Continuous imaging provides enhanced temporal resolution to reveal quantifiable fast adhesion dynamics. (A) Lung-metastatic 4T1 breast cancer cells (4T1-537) were transfected with mCherry–paxillin. Arrows follow adhesions with a slow assembly rate (red), medium assembly and disassembly rates (orange) and fast dynamics (green). Images were captured continuously for 20 min on an SD microscope with a 63×1.40 NA oil immersion objective lens. Camera exposure time was set to 5 s with 2×2 binning. Scale bar: 10 µm. (B) Fluorescence intensity traces of adhesions from A. Circles (●) are continuous imaging, squares (■) are every 20 s, and diamonds (♦) are every 30 s. (C) The total number of assembly (green) and disassembly (red) events detected for each cell imaged continuously (open circle; ○) compared to simulated data generated by duplicating every fourth (open square; □) or sixth (open diamond; ◇) image frame (n=6). A region of interest tool was used to selectively track adhesions in protrusive cell regions. *P<0.003 from continuous imaging; $^{\#}P$<0.005 from every 20 s (Mann–Whitney U-test). (D) Average assembly and disassembly rates for each data set depicted in C were determined from the rate of change in mean fluorescence intensity. Data represent the mean±s.e.m. for dynamic events pooled from six cells imaged for 20 min. Number of events analyzed is indicated in parentheses. *P<0.0001 from continuous imaging; $^{\#}P$<0.001 from every 20 s (Mann–Whitney U-test). (E,F) Frequency distribution of assembly and disassembly rates from D. Data values were binned into 0.06 min^{-1} segments. Boxed regions in each graph illustrate rapid adhesion dynamics only captured by continuous imaging. (G) NMuMG-ErbB2 cells expressing VinculinTS were continuously imaged for 20 min with a 448 nm laser. Cells were subsequently illuminated for another 20 min with a 491 nm laser. Scale bars: 10 µm for whole-cell images and 3 µm for magnified images. (H) Photobleaching decay curves of fixed NMuMG-ErbB2 cells with VinculinTS. Teal and venus bleaching experiments were conducted independently. Curves were normalized by the maximum fluorescence intensity of each experiment. Data represents the average of three independent experiments. Shaded areas represent mean±s.e.m.

Journal of Cell Science (2020) 133, jcs242834. doi:10.1242/jcs.242834

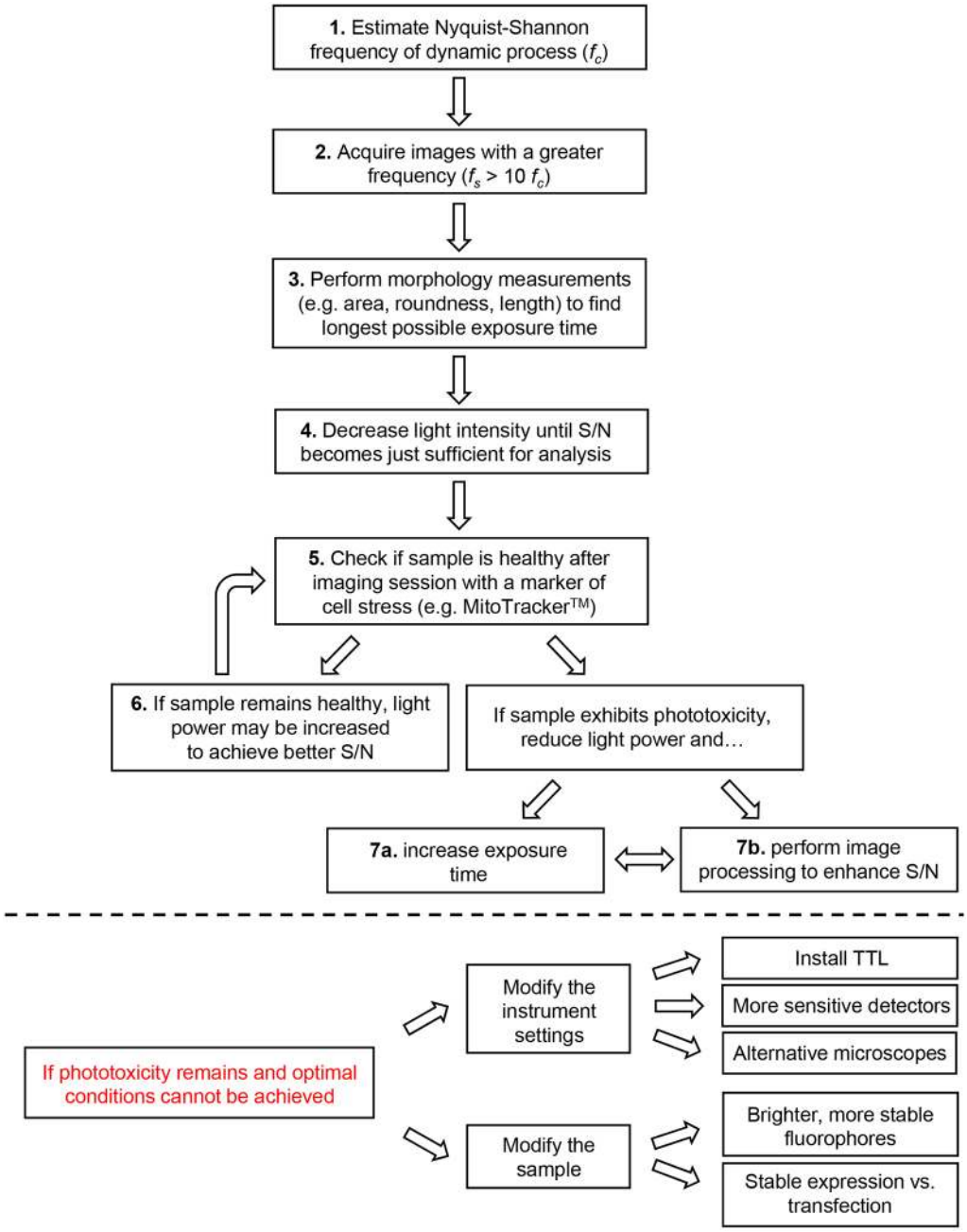

Fig. 7. Flowchart for optimizing live-cell fluorescence imaging. A workflow for determining exposure time and light power was developed based on the results of the current study. Implementing longer exposure times will help researchers establish optimal live-cell imaging conditions on microscopes without TTL.

decreases exponentially as exposure time increases. Finally, DLD can reveal cellular events with unprecedented detail and accuracy, which are not detected with previous CLD configurations.

To help researchers reduce photobleaching and phototoxicity on microscopes without TTL, and more generally, to determine ideal image acquisition limits, a workflow for optimizing exposure time and light power is presented (Fig. 7). Firstly, researchers should estimate the camera exposure time required to capture a given biological process based on the Nyquist–Shannon frequency of known dynamics (step 1). Images should then be acquired at a much higher frequency (step 2) to determine the longest exposure time that does not result in image artifacts (e.g. blur) (step 3). Interval delays should be eliminated to harness the entire interval time for gathering fluorescence emission and minimize the impact of hardware delays. Using this newly determined exposure time, light intensity should be reduced to the lowest possible power such that image S/N is still suitable for image analysis (e.g. identification of objects, or measurements of morphology and tracking) (step 4). In our experience, a S/N of 2 is typically required for thresholding and the identification of objects without the need for extensive image processing. A quick assay for cell health, such as end-point imaging of mitochondrial morphology, should then be performed to verify lack of phototoxicity and determine whether light levels are compatible with live-cell imaging (step 5). Finally, if cells are viable, light intensity may be increased incrementally until a compromise between S/N and cell viability is reached (step 6). If image quality (i.e. S/N) is insufficient with these conditions, image processing techniques can be applied (step 7). In the current study, we demonstrate the utility of median filtering, spatial binning and temporal binning; however, there are now many more advanced image processing techniques. Denoising filters (Carlton et al., 2010; Coupé et al., 2012), deconvolution (Biggs, 2010) or newer

machine-learning methods for denoising (Nasser and Boudier, 2019) and content-aware image restoration (Weigert et al., 2018) may also be applied to significantly improve S/N. These techniques can be particularly useful if object centers need to be tracked. However, the methods must be validated if quantitative measurements of structural area, volume, morphology or intensity are required.

Situations may arise where optimal conditions cannot be achieved. In these instances, the instrument or sample could be modified. First and foremost, researchers should consider implementing TTL on their microscope system if it is possible. IO may be difficult to overcome for very dynamic processes that require exceptionally short exposure times. Measuring the total exposure time with an oscilloscope will reveal the extent of IO. In addition, constitutive expression of brighter, more stable fluorophores can improve S/N by generating more emission light with the same excitation intensity. Alternatively, more sensitive detectors or different forms of microscopy can be used to capture more signal or deliver light in a less concentrated fashion (e.g. light sheet).

On microscopes without TTL, applying the concept of DLD will allow researchers to generate high S/N images with minimal phototoxicity, while retaining reasonable temporal resolution, to study a wide range of biological processes. Unfortunately, it is becoming increasingly difficult to employ lower light levels as light sources continue to be developed with higher power outputs. Moreover, commercial microscopes report illumination power in arbitrary percentage power rather than watts. Thus, seemingly small changes in percentage power may result in large changes in light power and have a dramatic effect on cell health. Access to light sources with refined control over incident light powers, and high stability at low power settings, would increase support for live-cell imaging and permit cell biologists to capture rapid cellular events with DLD illumination conditions.

MATERIALS AND METHODS

Cell culture

Wild-type Chinese Hamster Ovary-K1 (CHO-K1) cells were obtained from the American Type Culture Collection (cat. no.: CCL-61, ATCC). CHO-K1 cells stably expressing paxillin–EGFP were obtained from the lab of Dr Rick Horowitz (University of Virginia, Charlottesville, VA). CHO-K1 cells were grown in low glucose (1.0 g l^{-1}) Dulbecco's modified Eagle's medium (DMEM; cat. no. 11,885-084, Thermo Fisher Scientific) supplemented with 10% fetal bovine serum (FBS; cat. no. 10082-147, Thermo Fisher Scientific), 1% non-essential amino acids (cat. no. 11140-050, Thermo Fisher Scientific), 25 mM 4-(2-hydroxyethyl)-1-piperazineethanesulfonic acid (HEPES; cat. no. 15630-080, Thermo Fisher Scientific) and 1% penicillin-streptomycin (cat. no. 10378-016, Thermo Fisher Scientific). Cells were maintained in 0.5 mg ml^{-1} Geneticin-418 (G418; cat. no 11811-031, Thermo Fisher Scientific) antibiotic selection to maintain paxillin–EGFP expression.

Normal murine mammary gland (NMuMG) cells were obtained from the ATCC (cat. no. CRL-1636) and grown in high glucose (4.5 g l^{-1}) DMEM (cat. no. 319-005-CL, Wisent Bioproducts) supplemented with 5% FBS, 10 µg ml^{-1} insulin (cat. no. 511-016-CM, Wisent Bioproducts), 1 mM L-glutamine (cat. no. 609-065-CM, Wisent Bioproducts), 1% penicillin-streptomycin and 0.2% amphotericin B (cat. no. 450-105-QL, Wisent Bioproducts). NMuMG cells were infected with a pMSCV-blast viral vector harboring LifeAct-EGFP to label the actin cytoskeleton. Cells were maintained in 5 µg ml^{-1} blasticidin (cat. no. BLL-40-01, InvivoGen) antibiotic selection to maintain LifeAct–EGFP expression.

NMuMG-ErbB2 cells were previously generated in the laboratory of P.M.S. by infecting parental NMuMG cells with a pMSCV-hygromycin viral vector harboring the rat ortholog of ErbB2 with an activating transmembrane point mutation V664E (Ngan et al., 2013). NMuMG-ErbB2 cells were subsequently infected with a pMSCV-blast viral vector containing the vinculin tension sensor (VinculinTS) (Grashoff et al., 2010). Cells were cultured as described above with the addition of 0.8 mg ml^{-1} hygromycin B (cat. no. 450-141-XL, Wisent Bioproducts) antibiotic selection to maintain ErbB2 expression and 5 µg ml^{-1} blasticidin to maintain VinculinTS expression.

To generate explants 87 and 118, NMuMG-ErbB2 cells were injected into the mammary fat pad of athymic mice and subsequently explanted from primary tumors (Northey et al., 2008, 2013). Explant 118 was infected with a pMSCV-blast viral vector containing LifeAct–BFP. Cells were maintained in 5 µg ml^{-1} blasticidin to maintain LifeAct–BFP expression. In contrast, explant 87 was infected with a pMSCV-puromycin viral vector containing an shRNA against endogenous ShcA (an adapter protein involved in ErbB2 signaling). These cells were then infected with a pMSCV-blast viral vector harboring ShcA-iRFP. Cells were maintained in 2 µg ml^{-1} puromycin (cat. no. QLL-40-01, InvivoGen) to maintain knockdown and 5 µg ml^{-1} blasticidin to maintain re-expression.

Liver-metastatic (4T1-2776; Tabariès et al., 2011) and lung-metastatic (4T1-537; Rose et al., 2010) breast cancer cells were derived from 4T1 breast cancer cells, a model of triple-negative breast cancer. Both explants were grown in high glucose (4.5 g l^{-1}) DMEM supplemented with 10% FBS, 1% penicillin-streptomycin and 0.2% amphotericin B. 4T1-2776 cells were subsequently infected with mCherry–LPP using a pMSCV-blast viral vector and kept in 5 µg ml^{-1} blasticidin to maintain expression. In contrast, 4T1-537 cells were transiently transfected with pmCherry-paxillin (Addgene #50526).

Proximal kidney tubule (LLC-PK1) cells stably expressing EB3–mEmerald and H2B–mCherry were a gift from Michael W. Davidson (National High Magnet Laboratory, Florida State University, FL). LLC-PK1 cells were grown in DMEM-F12 (cat. no. 21331-020, Thermo Fisher Scientific) supplemented with 10% FBS, 15 mM HEPES, 1 mM L-glutamine and 1% penicillin-streptomycin.

Mycoplasma screening was routinely performed using MycoAlert mycoplasma detection kit (cat. no. LT07-318, Lonza). Cells were not authenticated following acquisition from the ATCC.

DNA constructs

All viruses were expressed using the MSCV vector system. To create NMuMG cells expressing BFP– and EGFP–LifeAct, *Nhe*I and *Not*I restriction sites were first used to clone mTagBFP-Lifeact-7 (Addgene #54496) into pSL301. *Bgl*II and *Xho*I restriction enzymes were then used to clone BFP-LifeAct into pMSCV-blast. Finally, *Bam*HI and *Not*I restriction enzymes were used to replace mTagBFP with EGFP from mGFP-Lifeact-7 (Addgene #54610).

To create NMuMG-ErbB2 cells expressing VinculinTS, *EcoR*I and *Hind*III restriction sites were used to clone VinculinTS (Addgene #26019) into pBlueScript. *Hind*III and *Xho*I restriction enzymes were then used to move VinculinTS into pMSCV-blast.

To create 2776-4T1 cells expressing mCherry–LPP, LPP was PCR-amplified from a previously generated construct (pMSCV-eGFP-WT-LPP; Ngan et al., 2017) with the following primers: 5′-ATTGCGGCCGCGATG-TCTCACCCATCTTGG-3′ and 5′-GAGACGTGCTACTTCCATTTGTC-3′. *EcoR*I and *Not*I restriction enzymes were then used to replace paxillin in a previously generated pMSCV-mCherry-paxillin construct with the amplified product.

To create NMuMG-ErbB2 cells expressing ShcA-iRFP, ShcA was PCR-amplified from a previously generated construct (pMSCV-ShcA-WT; Northey et al., 2013) with the following primers: 5′-CCCTTGAACCTCCT-CGTTCGACC-3′ and 5′-TAGGTACCGCCTTGTCATCGTCATCCT-3′. *Xho*I and *Kpn*I restriction enzymes were then used to insert the amplified product into pCMV-miRFP670 (Shcherbakova et al., 2016). Finally, 5′-CGCAAATGGGCGGTAGGCGTG-3′ and 5′-TATAGAATTCTTAGC-TCTCAAGCGCGG-3′ primers with *EcoR*1 and *Bgl*II restriction sites were used to shuttle ShcA-iRFP into pMSCV-blast. Retroviruses were generated in 293VSV cells according to the manufacturer's instructions (Clontech).

Cell migration assays

CHO-K1 cells expressing paxillin–EGFP were seeded onto µ-slide 8-well plates (cat. no. 80821, IBIDI) coated with 2 µg ml^{-1} (or 0.21 µg cm^{-2}) fibronectin (cat. no. F-0895, Sigma-Aldrich) diluted in 1× phosphate-

Journal of Cell Science (2020) 133, jcs242834. doi:10.1242/jcs.242834

buffered saline (PBS). Cells were allowed to adhere and grow under exponential conditions for at least 12 h prior to experimentation. Images were acquired on a Zeiss AxioObserver fully automated inverted microscope equipped with a Plan ApoChromat 20×0.8 NA objective, Axiocam 506 camera (Carl Zeiss, Jena, Germany) and Chamlide TC-L-Z003 stage top environmental control incubator (Live Cell Instrument, Seoul, South Korea). For baseline measurements of cell motility, cells were illuminated with a halogen lamp (HAL 100, Carl Zeiss). To determine the effects of fluorescence illumination, an EGFP filter cube (filter set 10; 450–490 nm excitation, 515–565 nm emission; Carl Zeiss) was used in combination with an X-Cite 120LED lamp (Excelitas Technologies, Waltham, MA) and several incident light powers. Camera exposure times were adjusted for each setting to maintain a constant number of photons impacting the sample during image acquisition (Table S2). The light source was directly triggered by USB or TTL without the use of a mechanical shutter. To test the effects of increasing light dose, CHO-K1 cells were illuminated more frequently (condensed light delivery; 61.6 mW×24 ms) or with increasing incident light power (diffuse light delivery; 0.0245 mW×60,000 ms) (Table S3). Images were acquired for at least 2 h.

In a similar manner, NMuMG-ErbB2 (118) with BFP-LifeAct, 4T1-2776 with mCherry-LPP and NMuMG-ErbB2 (87) with ShcA-iRFP cells were seeded onto µ-slide 8-well plates coated with 5 µg cm^{-2} fibronectin (Cat. no. FC010, EMD Millipore). Cells were imaged on the Zeiss AxioObserver with a Plan ApoChromat 20×0.8 NA objective. BFP–LifeAct was captured with brightfield, 33.90 mW for 24 ms, and 0.015 mW for 60,000 ms; mCherry–LPP cells were captured with brightfield, 58.40 mW for 100 ms, and 0.099 mW for 60,000 ms; and ShcA–iRFP was captured with brightfield, 33.90 mW for 24 ms, and 0.015 mW for 60,000 ms (Table S5). BFP excitation was delivered through a custom filter cube [365–395 nm excitation, long pass (LP) 420 nm emission]; mCherry excitation was delivered through filter set 00 (530–585 nm excitation, LP 615 nm emission; Carl Zeiss); and iRFP excitation was delivered through filter set 49006 (590–650 nm excitation, 662.5-737.5 nm emission; Chroma). Images were acquired every minute for a total of 3 h.

Analysis of cell migration

Cells were manually tracked in ImageJ (NIH, Bethesda, MD) using the manual tracking plugin. The center of the nucleus was used as the reference point for each cell. User bias was minimized by having several authors track the cells. *x*,*y* position data for each cell track was then exported to MATLAB (v. 8.6, Rel. R2015b; The MathWorks, Natick, MA). Rose plots of cell movement were created by superimposing the starting position of each track on the origin (0,0). The average speed of each 10-min segment was then calculated by determining the mean distance traveled between each time point over the imaging interval. The average speed of each cell was calculated in a similar fashion. The data shown represents the mean±standard error of the mean (s.e.m.) for all cells analyzed from three independent experiments.

Mitochondrial morphology following cell tracking experiments

CHO-K1 cells expressing paxillin–EGFP were stained with 100 nM MitoTracker™ Red CMXRos (cat. no. M7512, Thermo Fisher Scientific) for 10 min. Cells were then fixed with 4% PFA preheated to 37°C for 10 min, washed with PBS and kept in PBS solution. As a negative control, cells that did not receive fluorescence illumination were also stained and fixed. Similarly, cells treated with 250 µM H_2O_2 (cat. no. 216763, Sigma-Aldrich) for 3 h were included as a positive control. Note that the 0.0245 mW condition depicts cells imaged continuously (60,000 ms) for 16 h. Images of mitochondrial morphology were acquired on a Leica DMI6000B inverted microscope equipped with a Quorum WaveFx-X1 spinning disk confocal system (Quorum Technologies, Guelph, ON), HCX PL APO 63×1.40 NA oil DIC objective, and two Prime BSI sCMOS cameras (Photometrics, Tucson, AZ). Each cell was illuminated with 491 and 561 nm diode lasers to capture paxillin–EGFP and MitoTracker™ Red signals, respectively. The pinhole size of the spinning disk was fixed at 50 µm.

Mitochondrial morphology during cell-tracking experiments

CHO-K1 cells expressing paxillin–EGFP were seeded onto µ-dish 35 mm high glass bottom dishes (cat. no. 81158, IBIDI) coated with 0.21 µg cm^{-2} fibronectin. Cells were allowed to adhere and grow under exponential conditions for at least 12 h. Cells were then stained with 50 nM MitoTracker™ Red diluted in cell culture medium (pre-heated to 37°C) for 10 min. After staining, cells were washed once with fresh medium and placed in new cell culture medium for imaging. Images were acquired on the Zeiss AxioObserver with a PlanApo 63×1.4 NA oil immersion objective. Paxillin–EGFP was excited every minute with 0.0093 mW or 21.3 mW of incident light (Table S4). Exposure time was set to 60,000 ms for the low-power condition and 24 ms for the high-power condition. MitoTracker™ Red was excited every 6 min with a total light dose of 360 mW×ms using filter set 43 (532.5–557.5 nm excitation, 570–640 nm emission; Carl Zeiss). The 120LED light source was activated through a USB connection. Images were subsequently imported into ImageJ to assess cell and mitochondrial morphology over time. Cell area was determined by manually outlining each cell. In contrast, analysis of mitochondrial morphology required several pre-processing steps. Briefly, we applied (1) a despeckling filter, (2) enhanced local contrast (CLAHE) with blocksize 9 and maximum slope 4 and (3) sharpened the image. This image was then (4) duplicated and (5) mean filtered with a 10×10 grid. Finally, the duplicated image was subtracted from the enhanced image (3–5) and imported into Imaris (v. 9.1.2; Bitplane AG, Zurich, CH) to analyze mitochondrial area with the Surfaces function. Detail from the surfaces function was smoothed and set to 0.140 µm with a local background subtraction of 0.140 µm. Surfaces smaller than 3 voxels were removed by filtering. Measurements for cell and mitochondrial area were normalized to initial values. The data shown represents the mean±s.e.m. for five cells from three independent experiments.

Photobleaching assays for paxillin–EGFP

CHO-K1 cells expressing paxillin–EGFP were seeded onto µ-slide 8-well plates and fixed with PFA. Images were acquired on the Zeiss AxioObserver microscope with a Plan ApoChromat 20×0.8 NA objective. Cells were repeatedly imaged for at least 300 frames with different illumination conditions. Camera exposure times were adjusted for each setting to maintain a constant number of photons impacting the sample during image acquisition (Table S2). The light source was directly triggered by USB or TTL without the use of a mechanical shutter. Definite Focus.2 (Carl Zeiss, Jena, Germany) was used to keep the *z*-focus constant throughout the experiment. Image drift in *x*,*y* was corrected in Imaris by tracking the position of an adhesion over time relative to the first frame. Image stacks were subsequently analyzed in ImageJ. Three regions of interest (30×30 pixels) were drawn and averaged to determine intensity decay over time for each condition. A 50×50 pixel region of interest was used to correct decay curves for fluctuations in background intensity. Curves were normalized by the maximum fluorescence intensity of each experiment. The data shown represents the mean±s.e.m. for three independent experiments.

ROS production in response to different illumination conditions

CHO-K1 cells expressing paxillin–EGFP were seeded onto µ-slide 8-well plates. Cells were stained with 0.83 µM CellRox™ Deep Red Reagent (cat. no. C10422, Thermo Fisher Scientific). Images were taken on the Zeiss AxioObserver with a Plan ApoChromat 20×0.8 NA objective (TTL triggering) or a PlanApo 63×1.4 NA objective (USB triggering). CellRox™ was imaged before and after paxillin–EGFP photobleaching (400 frames) with a total light dose of 1030 mW×ms delivered through filter set 49006 (590–650 nm excitation, 662.5–737.5 nm emission; Chroma). Exposure time was set to 1000 ms. ImageJ was used to determine the mean intensity of CellROX™ in each cell. The data shown represents the mean± s.e.m. for nine cells from three independent experiments.

To determine ROS production as a function of total light dose, paxillin–EGFP photobleaching was performed with increasing incident light powers. Camera exposure time for paxillin–EGFP was set to 100 ms. Changes in CellROX™ intensity were performed as described above.

Signal-to-noise ratio of widefield images

CHO-K1 cells expressing paxillin–EGFP were seeded onto µ-slide 8-well plates and fixed with PFA. Cells were subsequently stained with DAPI diluted to 0.5 mg ml^{-1} in water. Images were acquired on the Zeiss AxioObserver with a 20×0.8 NA objective and 15 illumination settings (Tables S2 and S3).

Journal of Cell Science (2020) 133, jcs242834. doi:10.1242/jcs.242834

For each setting, the same field of view was captured to directly compare S/N (Tables S6 and S7). A single DAPI image was taken with 100 ms exposure time using filter set 49 (365 nm excitation, 420–470 nm emission; Carl Zeiss). Images were then analyzed in MetaXpress using the multi wavelength cell scoring application. Briefly, the minimum and maximum width of nuclei was set to 10 and 32 µm, respectively, while minimum and maximum width of the cytoplasm was set to 2.3 and 90.8 µm, respectively. Finally, the mean intensity of each cell was background subtracted and divided by the standard deviation of the background (σ_{bkg}). σ_{bkg} was determined from a 125×125 pixel region of interest without cells. The data shown represents the mean±s.e.m. for three independent experiments.

IO severely impacts image quality of dynamic processes

LLC-PK1 cells stably expressing EB3–mEmerald and H2B–mCherry were seeded onto 35 mm glass-bottom dishes (cat. no. FD35, World Precision Instruments; WPI) coated with 5 µg cm^{-2} fibronectin. Cells were allowed to adhere and grow under exponential conditions for at least 12 h prior to experimentation. Cells were then imaged with an HCX PL APO 63×1.40 NA oil objective on the spinning disk confocal system described above. A CU-501 stage-top incubator system (Live Cell Instrument, Seoul, South Korea) was used to maintain cells in a 37°C environment with 5% CO_2. Images of EB3-mEmerald were captured with 10 different illumination settings (Table S8). Imaris was then used to determine the S/N of EB3. Detail from the surfaces function was smoothed and set to 0.150 µm with a local background subtraction of 0.300 µm. Manual refinement of the autothreshold feature was used to mask EB3 tip proteins. Finally, surfaces smaller than 10 voxels were removed by filtering. The mean intensity of EB3–mEmerald in each image was background subtracted and divided by σ_{bkg} (250×250 pixel region of interest).

Cells were then continuously imaged for 2 min with an exposure time of 400 ms and a variety of laser powers to evaluate photobleaching (0.0167, 0.031, 0.0517, 0.0914, 0.181, 0.333, 0.558 and 0.922 mW). Stream to RAM acquisition was used in MetaMorph (Molecular Devices, Sunnyvale, CA) to minimize the delay in saving images. Initial and final mean intensities of EB3–mEmerald were determined using Imaris. Initial intensity was set to 1. The data shown represents the mean±s.e.m. for at least three independent experiments.

Determining the maximum exposure time for microtubule dynamics

LLC-PK1 cells expressing EB3–mEmerald and H2B–mCherry were seeded onto 35 mm dishes (WPI). EB3–mEmerald was rapidly imaged with a 10 ms exposure time for a total of 5.005 s (stream acquisition). A 491 nm laser set to 1.35 mW was used to capture sufficient S/N for morphology analysis. Image stacks were imported into ImageJ to generate maximum intensity projections corresponding to exposure times of 37, 64, 91, 199, 388, 496, 604, 1009, 1495, 2008, 3007, 3493, 4006, 4492 and 5005 ms. These images were then imported into Imaris (including the first 10 ms exposure) to determine the area, roundness and length of EB3 (see parameters above). Values were normalized on a scale of 0–1. The data shown represents the mean±s.e.m. for five independent experiments.

Dual-color imaging of EB3-mEmerald and H2B-mCherry

LLC-PK1 cells were continuously illuminated for over 2 min with the 491 nm laser set to 0.020 mW and a 561 nm diode laser set to 0.010 mW (Table S9). A dichroic mirror set to reflect light below, and pass light above, 565 nm, combined with a 565 nm long pass filter (Chroma Technologies, Bellows Falls, VT) was used to send the emission signals to two separate Prime BSI sCMOS cameras and thereby capture both signals simultaneously. Camera exposure times were set to 200 ms.

Effect of image processing on EB3 morphology

EB3–mEmerald images captured with a 10 ms exposure time for a total of 5.005 s (stream acquisition) were summed in ImageJ to generate exposure times of 37, 64, 91, 199 and 388 ms. A 2×2 median filter was then applied to the images (including the first 10 ms exposure). Raw and filtered images were analyzed in Imaris to determine the area, roundness and length of EB3 (see parameters above). Measurements determined from filtered images were normalized to values calculated from raw data to determine relative changes in morphology. Values greater or less than 1.5 times the standard deviation were considered outliers. S/N was determined as described above. Linescan analysis was used to visually show the signal for each exposure time before and after filtering.

Tracking microtubule tip-binding proteins

Dual-color image stacks were loaded into Imaris and analyzed using the Spots function. The estimated *xy* diameter for EB3–mEmerald was set to 0.650 µm with background subtraction enabled. A quality filter was then used to select positive signals. Finally, tip proteins were tracked using an autoregressive algorithm with a maximum distance of 0.800 µm and gap size of 3 time points. Tracks shorter than 4 s were removed by filtering. Finally, a custom algorithm in MATLAB was used to determine the average speed of each tip protein from *x*,*y* position data.

Imaging mitochondrial and lysosomal dynamics

CHO-K1 cells were seeded onto µ-slide 8-well plates and stained with 100 nM MitoTracker™ Red or 500 nM LysoTracker™ Green DND-26 (Cat. no. L7526, Thermo Fisher Scientific) for 10 min. Images were acquired with an HCX PL APO 63×1.40 NA oil objective on the spinning disk confocal system. Each cell was illuminated for ∼5 min with the 561 nm diode laser set to 0.037 mW (MitoTracker™ Red) or the 491 nm laser set to 0.020 mW (LysoTracker™ Green) (Table S9). Camera exposure time was set to 100 ms.

Analysis of mitochondrial and lysosomal dynamics

MitoTracker™ Red and LysoTracker™ Green image stacks were imported into ImageJ. Spatial binning (or addition) was accomplished by summing 2×2, 3×3 or 4×4 pixels within the same image. Temporal binning was accomplished by summing 2, 4 or 8 images. Lysosomal images were then loaded into Imaris for morphology analysis. Detail from the surfaces function was smoothed and set to 0.100 µm with a local background subtraction of 0.200 µm. Manual refinement of the autothreshold feature was then used to mask lysosomes. Finally, splitting touching objects was set to a seed points diameter of 0.500 µm. The data shown represents the mean±s.e.m. for five cells from four independent experiments.

Three-dimensional imaging of mitochondrial dynamics

CHO-K1 cells were seeded onto µ-slide 8-well plates and stained with 50 nM MitoTracker™ Red for 10 min. Images were acquired with an HCX PL APO 63×/1.40NA oil objective on the spinning disk confocal system. Cells were continuously imaged for over 5 min. *Z*-stacks with a step size of 0.25 µm were captured as frequently as possible (1.74–1.88 s) to observe mitochondrial volume over time. An MS-2000 piezo stage (ASI, Eugene, OR) and stream acquisition were used to capture focal planes with minimal IO. Camera exposure time was set to 50 ms with 2×2 pixel binning.

3D image stacks were imported into Imaris to mask mitochondrial volume. Detail from the surfaces function was smoothed and set to 0.180 µm with a local background subtraction of 0.350 µm. Manual refinement of the autothreshold feature was then used to mask mitochondria. Surfaces smaller than 10 voxels were removed by filtering. Finally, mitochondrial networks were statistically coded for volume using a spectrum colormap.

Imaging adhesion dynamics

Lung-metastatic 4T1 breast cancer cells (4T1-537) were seeded onto 35 mm dishes (WPI) coated with 5 µg cm^{-2} fibronectin. Cells were transfected with 1 µg of pmCherry–paxillin using Effectine reagent (cat. no. 301425, QIAGEN) and allowed to recover for an additional 24 h before imaging. Images were acquired with an HCX PL APO 63×1.40 NA oil objective on the spinning disk confocal system; however, an ORCA-Flash4.0 sCMOS camera (Hamamatsu Photonics K.K., Hamamatsu City, Japan) was used in this set of experiments. Each cell was continuously illuminated for 20 min with a 561 nm diode laser set to 0.031 mW (Table S9). Camera exposure time was set to 5 s with 2×2 pixel binning.

Similarly, CHO-K1 cells expressing paxillin–EGFP were seeded onto 35 mm dishes (WPI) coated with 0.21 µg cm^{-2} fibronectin. Each cell was continuously illuminated for 20 min with a 491 nm diode laser set to 0.016 mW (Table S9). Camera exposure time was set to 5 s with 2×2 pixel binning.

Journal of Cell Science (2020) 133, jcs242834. doi:10.1242/jcs.242834

Processing adhesion dynamics data

To remove hot pixels and other sources of background noise, an area of the sample without cells was acquired for 8.75 min. A maximum intensity projection of this image stack was created to extract only the persistent noise pixels. This 'hot' pixel noise image was then subtracted from the raw data. To simulate data captured every 20 or 30 s, every fourth or sixth image was duplicated into a new image stack, respectively.

Tracking adhesions

Each image stack was loaded into Imaris to analyze adhesion dynamics with the Surfaces function. A protruding edge of each cell was manually selected using the region of interest tool. Detail from the surfaces function was smoothed and set to 0.200 µm with a local background subtraction of 0.200 µm. Adhesions were then masked by a manual refinement of the autothreshold feature. Splitting touching objects was set to a seed points diameter of 0.500 µm. Finally, adhesions were tracked over time using an autoregressive algorithm with a maximum distance of 0.700 µm and maximum gap size of three time points. Surfaces smaller than 5 voxels were removed by filtering. Note that for each cell, the same parameters used to analyze the continuous series were applied to the simulated 20 and 30 s interval series to ensure consistency.

Calculating adhesion dynamics

Mean intensity data for each adhesion tracked in Imaris was exported to MATLAB for further analysis. A spline curve was first fitted to each intensity trace to identify segments of assembly and disassembly. The difference in intensity between each time point was calculated, and changes greater than 20% were considered to be significant. A string of six or more points upwards was interpreted as assembly, while six of more points downwards was interpreted as disassembly. A log-linear fitting method was then used to determine the rate for each event. Fits with an R^2 value greater than 0.7 were considered to be significant. Finally, assembly and disassembly rates were pooled together to determine the mean±s.e.m. rate for each condition.

Imaging actin cytoskeleton dynamics

NMuMG cells stably expressing LifeAct–EGFP were seeded onto 35 mm dishes (WPI). Images were acquired with an HCX PL APO 63×1.40 NA oil objective on the spinning disk confocal system. Each cell was continuously illuminated for 30 min with the 491 nm diode laser set to 0.060 mW (Table S9). The camera exposure time was set to 5 s with 2×2 pixel binning.

Dual-color imaging of adhesion and cytoskeleton dynamics

CHO-K1 cells stably expressing paxillin–EGFP were transfected with 1 µg of LifeAct–mRuby (Addgene #54560) using Lipofectamine 2000 reagent (cat. no. 11668027; Thermo Fisher Scientific). Cells were then seeded onto 35 mm dishes (WPI). Images were acquired with an HCX PL APO 63×1.40 NA oil objective on the spinning disk confocal system. Each cell was continuously illuminated for 20 min with the 491 nm laser set to 0.016 mW and the 561 nm diode laser set to 0.031 mW (Table S9). A dichroic mirror set was used to send the emission signals to two separate cameras. Camera exposure times were set to 5 s with 2×2 pixel binning.

Continuous illumination of less stable fluorescent proteins

NMuMG-ErbB2 cells stably expressing VinculinTS were seeded onto 35 mm dishes (WPI). Images were acquired with an HCX PL APO 63×1.40 NA oil objective on the spinning disk confocal system. Each cell was continuously illuminated for 20 min with a 448 nm laser set to 0.013 mW to image teal fluorescent protein. Immediately following this, cells were illuminated for another 20 min with the 491 nm laser set to 0.007 mW to image venus fluorescent protein (Table S9). Camera exposure time was set to 5 s with 2×2 pixel binning.

Photobleaching assays for all other fluorescent dyes and proteins

Cells were fixed with PFA immediately following live-cell imaging. Images were acquired on the spinning disk confocal system with the same settings used to acquire live-cell data. Three separate image stacks were collected for each condition. Three regions of interest (100×100 pixels) were drawn and averaged for each stack to determine the intensity decay over time. For relative comparison, photobleaching curves were normalized by the maximum fluorescence intensity of each experiment.

Measurements of exposure time

A digital oscilloscope (DS1054Z; Rigol, Beijing, China) coupled to a DET36A/M Si Based Detector (Thorlabs, Dachau, Germany) was used measure the total illumination time delivered by the mechanical shutter, USB or TTL light source activation. Voltage values were normalized on a scale of 0–1 and plotted in MATLAB.

Power measurements

An X-Cite optical power measurement system (XR2100) with an XP750 external sensor (Excelitas Technologies) was used to measure incident light intensity through air objectives (Plan ApoChromat 20×0.8 NA on the widefield microscope). A PM400 Optical Power and Energy Meter with an S170C Microscope Slide Power Sensor (Thorlabs) was used to measure incident light intensity through oil objectives (PlanApo 63×1.4 NA on the widefield microscope; HCX PL APO 63×1.40 NA on the spinning disk confocal system).

Power density measurements

Cells were seeded onto 35 mm glass-bottom dishes (WPI) coated with fluorescently conjugated gelatin (Oregon Green 488; cat. no. G13186, Invitrogen), as previously described (Ngan et al., 2017). Cells were then fixed with PFA and used to focus the desired objective lens (20×0.8 NA and 63×1.4 NA on the widefield microscope; 63×1.40 NA on the spinning disk confocal system). Fluorescent gelatin was photobleached with high-power light for at least 1 min. Finally, a lower magnification lens (5× or 10×) was used to capture an image of the photobleached area. Measurements of illumination area for each objective were performed in ImageJ.

Statistical analyses

In vitro experiments were performed at least three times. An $n\approx30$ was chosen for cell migration experiments to account for normal distribution. Statistical significance values (*P*-values) were obtained by performing an unpaired two-tailed Student's *t*-test or Mann–Whitney *U*-test. Data are presented as mean±s.e.m. Values were normalized where indicated.

Code availability

Contact A.K. for access to custom codes used in this article.

Acknowledgements

We thank the late Dr Michael W. Davidson (National High Magnet Laboratory, Florida State University, FL) for providing LLC-PK1 cells stably expressing EB3–mEmerald and H2B–mCherry. We also thank Rebecca Flessner (McGill University, QC) and members of the Brown and Siegel laboratories for thoughtful discussions about the manuscript. We thank the following imaging facilities for participating in the Canada BioImaging (CBI) survey: Cell Imaging Facility, CHUM Research Center; Molecular and Cellular Microscopy Platform (MCMP), Douglas Hospital Research Center; CAMiLoD, University of Toronto; Genomic Centre for Cancer Research and Diagnosis, University of Manitoba; Biology Microscopy Core, University of Saskatchewan; Platforme de microscopie photonique, University of Sherbrooke; Centre for Microscopy and Cellular Imaging, Concordia University; BMM Microscopy, University of Montreal; Neuro Microscopy Imaging Centre, Montreal Neurological Institute; MultiScale Imaging Facility, McGill University; Platforme d'Imagerie Microscopique, CHU Sainte-Justine Research Centre; Advanced Optical Microscopy Facility (AOMF), University Health Network. Imaging experiments were performed at the McGill Life Sciences Complex Advanced BioImaging Facility (ABIF) and Cell Imaging and Analysis Network (CIAN).

Competing interests

The authors declare no competing or financial interests.

Author contributions

Conceptualization: A.K., C.M.B.; Methodology: A.K., C.M.B.; Validation: A.K., E.V.; Formal analysis: A.K., E.V., F.M.; Investigation: A.K.; Data curation: A.K.; Writing - original draft: A.K., C.M.B.; Writing - review & editing: A.K., E.V., P.M.S., C.M.B.; Visualization: A.K.; Supervision: P.M.S., C.M.B.; Project administration: C.M.B.; Funding acquisition: P.M.S., C.M.B.

Funding
Work performed in the author's laboratories (P.M.S., C.M.B.) was supported by grants from Natural Sciences and Engineering Research Council of Canada (NSERC) (grants #493616-16, #386084-12), Canadian Institutes of Health Research (CIHR) (grant #CPG-146475) and the Canadian Cancer Society Research Institute CCS i2I grant #705838. A.K. acknowledges support in the form of a Fonds de Recherche du Québec - Santé (FRQS) doctoral studentship. E.V. acknowledges support in the form of CIHR and FRQS master's studentships. P.M.S. is a McGill University William Dawson Scholar.

Supplementary information
Supplementary information available online at
http://jcs.biologists.org/lookup/doi/10.1242/jcs.242834.supplemental

References
Albeanu, D. F., Soucy, E., Sato, T. F., Meister, M. and Murthy, V. N. (2008). LED arrays as cost effective and efficient light sources for widefield microscopy. *PLoS ONE* **3**, e2146. doi:10.1371/journal.pone.0002146
Alejo, J. L., Blanchard, S. C. and Andersen, O. S. (2013). Small-molecule photostabilizing agents are modifiers of lipid bilayer properties. *Biophys. J.* **104**, 2410-2418. doi:10.1016/j.bpj.2013.04.039
Baird, T. R., Kaufman, D. and Brown, C. M. (2014). Mercury free microscopy: an opportunity for core facility directors. *J. Biomol. Tech.* **25**, 48-53. doi:10.7171/jbt.14-2502-001
Berginski, M. E., Vitriol, E. A., Hahn, K. M. and Gomez, S. M. (2011). High-resolution quantification of focal adhesion spatiotemporal dynamics in living cells. *PLoS ONE* **6**, e22025. doi:10.1371/journal.pone.0022025
Biggs, D. S. (2010). 3D deconvolution microscopy. *Curr. Protoc. Cytom.* **52**, 12.19.1-12.9.20. doi:10.1002/0471142956.cy1219s52
Bogdanov, A. M., Bogdanova, E. A., Chudakov, D. M., Gorodnicheva, T. V., Lukyanov, S. and Lukyanov, K. A. (2009). Cell culture medium affects GFP photostability: a solution. *Nat. Methods* **6**, 859-860. doi:10.1038/nmeth1209-859
Bogdanov, A. M., Kudryavtseva, E. I. and Lukyanov, K. A. (2012). Anti-fading media for live cell GFP imaging. *PLoS ONE* **7**, e53004. doi:10.1371/journal.pone.0053004
Carlton, P. M., Boulanger, J., Kervrann, C., Sibarita, J.-B., Salamero, J., Gordon-Messer, S., Bressan, D., Haber, J. E., Haase, S., Shao, L. et al. (2010). Fast live simultaneous multiwavelength four-dimensional optical microscopy. *Proc. Natl. Acad. Sci. USA* **107**, 16016-16022. doi:10.1073/pnas.1004037107
Choi, C. K., Vicente-Manzanares, M., Zareno, J., Whitmore, L. A., Mogilner, A. and Horwitz, A. R. (2008). Actin and alpha-actinin orchestrate the assembly and maturation of nascent adhesions in a myosin II motor-independent manner. *Nat. Cell Biol.* **10**, 1039-1050. doi:10.1038/ncb1763
Coupé, P., Munz, M., Manjón, J. V., Ruthazer, E. S. and Collins, D. L. (2012). A CANDLE for a deeper in vivo insight. *Med. Image Anal.* **16**, 849-864. doi:10.1016/j.media.2012.01.002
Delorme-Walker, V. D., Peterson, J. R., Chernoff, J., Waterman, C. M., Danuser, G., DerMardirossian, C. and Bokoch, G. M. (2011). Pak1 regulates focal adhesion strength, myosin IIA distribution, and actin dynamics to optimize cell migration. *J. Cell Biol.* **193**, 1289-1303. doi:10.1083/jcb.201010059
Dixit, R. and Cyr, R. (2003). Cell damage and reactive oxygen species production induced by fluorescence microscopy: effect on mitosis and guidelines for non-invasive fluorescence microscopy. *Plant J.* **36**, 280-290. doi:10.1046/j.1365-313X.2003.01868.x
Douthwright, S. and Sluder, G. (2017). Live cell imaging: assessing the phototoxicity of 488 and 546 nm light and methods to alleviate it. *J. Cell. Physiol.* **232**, 2461-2468. doi:10.1002/jcp.25588
Ettinger, A. and Wittmann, T. (2014). Fluorescence live cell imaging. *Methods Cell Biol.* **123**, 77-94. doi:10.1016/B978-0-12-420138-5.00005-7
Fiszer-Kierzkowska, A., Vydra, N., Wysocka-Wycisk, A., Kronekova, Z., Jarz?b, M., Lisowska, K. M. and Krawczyk, Z. (2011). Liposome-based DNA carriers may induce cellular stress response and change gene expression pattern in transfected cells. *BMC Mol. Biol.* **12**, 27. doi:10.1186/1471-2199-12-27
Frigault, M. M., Lacoste, J., Swift, J. L. and Brown, C. M. (2009). Live-cell microscopy - tips and tools. *J. Cell Sci.* **122**, 753-767. doi:10.1242/jcs.033837
Grashoff, C., Hoffman, B. D., Brenner, M. D., Zhou, R., Parsons, M., Yang, M. T., McLean, M. A., Sligar, S. G., Chen, C. S., Ha, T. et al. (2010). Measuring mechanical tension across vinculin reveals regulation of focal adhesion dynamics. *Nature* **466**, 263-266. doi:10.1038/nature09198
Icha, J., Weber, M., Waters, J. C. and Norden, C. (2017). Phototoxicity in live fluorescence microscopy, and how to avoid it. *Bioessays* **39**, 1700003. doi:10.1002/bies.201700003
Karbowski, M. and Youle, R. J. (2003). Dynamics of mitochondrial morphology in healthy cells and during apoptosis. *Cell Death Differ.* **10**, 870-880. doi:10.1038/sj.cdd.4401260
Knight, M. M., Roberts, S. R., Lee, D. A. and Bader, D. L. (2003). Live cell imaging using confocal microscopy induces intracellular calcium transients and cell death. *Am. J. Physiol. Cell Physiol.* **284**, C1083-C1089. doi:10.1152/ajpcell.00276.2002
Knoll, S. G., Ahmed, W. W. and Saif, T. A. (2015). Contractile dynamics change before morphological cues during fluorescence [corrected] illumination. *Sci. Rep.* **5**, 18513. doi:10.1038/srep18513
Komarova, Y., De Groot, C. O., Grigoriev, I., Gouveia, S. M., Munteanu, E. L., Schober, J. M., Honnappa, S., Buey, R. M., Hoogenraad, C. C., Dogterom, M. et al. (2009). Mammalian end binding proteins control persistent microtubule growth. *J. Cell Biol.* **184**, 691-706. doi:10.1083/jcb.200807179
Laissue, P. P., Alghamdi, R. A., Tomancak, P., Reynaud, E. G. and Shroff, H. (2017). Assessing phototoxicity in live fluorescence imaging. *Nat. Methods* **14**, 657-661. doi:10.1038/nmeth.4344
Laloi, C. and Havaux, M. (2015). Key players of singlet oxygen-induced cell death in plants. *Front. Plant Sci.* **6**, 39. doi:10.3389/fpls.2015.00039
Magidson, V. and Khodjakov, A. (2013). Circumventing photodamage in live-cell microscopy. *Methods Cell Biol.* **114**, 545-560. doi:10.1016/B978-0-12-407761-4.00023-3
Mubaid, F. and Brown, C. M. (2017). Less is more: longer exposure times with low light intensity is less photo-toxic. *Microsc. Today* **25**, 26-35. doi:10.1017/S1551929517000980
Murray, J. M. (1998). Evaluating the performance of fluorescence microscopes. *J. Microsc.* **191**, 128-134. doi:10.1046/j.1365-2818.1998.00374.x
Nasser, L. and Boudier, T. (2019). A novel generic dictionary-based denoising method for improving noisy and densely packed nuclei segmentation in 3D time-lapse fluorescence microscopy images. *Sci. Rep.* **9**, 5654. doi:10.1038/s41598-019-41683-3
Nayal, A., Webb, D. J., Brown, C. M., Schaefer, E. M., Vicente-Manzanares, M. and Horwitz, A. R. (2006). Paxillin phosphorylation at Ser273 localizes a GIT1-PIX-PAK complex and regulates adhesion and protrusion dynamics. *J. Cell Biol.* **173**, 587-589. doi:10.1083/jcb.200509075
Ngan, E., Northey, J. J., Brown, C. M., Ursini-Siegel, J. and Siegel, P. M. (2013). A complex containing LPP and alpha-actinin mediates TGFbeta-induced migration and invasion of ErbB2-expressing breast cancer cells. *J. Cell Sci.* **126**, 1981-1991. doi:10.1242/jcs.118315
Ngan, E., Stoletov, K., Smith, H. W., Common, J., Muller, W. J., Lewis, J. D. and Siegel, P. M. (2017). LPP is a Src substrate required for invadopodia formation and efficient breast cancer lung metastasis. *Nat. Commun.* **8**, 15059. doi:10.1038/ncomms15059
Northey, J. J., Chmielecki, J., Ngan, E., Russo, C., Annis, M. G., Muller, W. J. and Siegel, P. M. (2008). Signaling through ShcA is required for transforming growth factor beta- and Neu/ErbB-2-induced breast cancer cell motility and invasion. *Mol. Cell. Biol.* **28**, 3162-3176. doi:10.1128/MCB.01734-07
Northey, J. J., Dong, Z., Ngan, E., Kaplan, A., Hardy, W. R., Pawson, T. and Siegel, P. M. (2013). Distinct phosphotyrosine-dependent functions of the ShcA adaptor protein are required for transforming growth factor beta (TGFbeta)-induced breast cancer cell migration, invasion, and metastasis. *J. Biol. Chem.* **288**, 5210-5222. doi:10.1074/jbc.M112.424804
Ott, M., Robertson, J. D., Gogvadze, V., Zhivotovsky, B. and Orrenius, S. (2002). Cytochrome c release from mitochondria proceeds by a two-step process. *Proc. Natl. Acad. Sci. USA* **99**, 1259-1263. doi:10.1073/pnas.241655498
Rose, A. A. N., Annis, M. G., Dong, Z., Pepin, F., Hallett, M., Park, M. and Siegel, P. M. (2010). ADAM10 releases a soluble form of the GPNMB/Osteoactivin extracellular domain with angiogenic properties. *PLoS ONE* **5**, e12093. doi:10.1371/journal.pone.0012093
Salmon, W. C. and Waters, J. C. (2011). CCD cameras for fluorescence imaging of living cells. *Cold Spring Harb. Protoc.* **2011**, 790-802. doi:10.1101/pdb.top113
Shaner, N. C., Steinbach, P. A. and Tsien, R. Y. (2005). A guide to choosing fluorescent proteins. *Nat. Methods* **2**, 905-909. doi:10.1038/nmeth819
Shcherbakova, D. M., Baloban, M., Emelyanov, A. V., Brenowitz, M., Guo, P. and Verkhusha, V. V. (2016). Bright monomeric near-infrared fluorescent proteins as tags and biosensors for multiscale imaging. *Nat. Commun.* **7**, 12405. doi:10.1038/ncomms12405
Spring, K. R. (2007). Cameras for digital microscopy. *Methods Cell Biol.* **81**, 171-186. doi:10.1016/S0091-679X(06)81010-1
Stennett, E. M. S., Ciuba, M. A. and Levitus, M. (2014). Photophysical processes in single molecule organic fluorescent probes. *Chem. Soc. Rev.* **43**, 1057-1075. doi:10.1039/C3CS60211G
Stepanova, T., Slemmer, J., Hoogenraad, C. C., Lansbergen, G., Dortland, B., De Zeeuw, C. I., Grosveld, F., van Cappellen, G., Akhmanova, A. and Galjart, N. (2003). Visualization of microtubule growth in cultured neurons via the use of EB3-GFP (end-binding protein 3-green fluorescent protein). *J. Neurosci.* **23**, 2655-2664. doi:10.1523/JNEUROSCI.23-07-02655.2003
Swedlow, J. R., Andrews, P. D. and Platani, M. (2009). In vivo imaging of mammalian cells: image acquisition and analysis. *Cold Spring Harb. Protoc.* **2009**, pdb ip70. doi:10.1101/pdb.ip70
Tabariès, S., Dong, Z., Annis, M. G., Omeroglu, A., Pepin, F., Ouellet, V., Russo, C., Hassanain, M., Metrakos, P., Diaz, Z. et al. (2011). Claudin-2 is selectively enriched in and promotes the formation of breast cancer liver metastases through engagement of integrin complexes. *Oncogene* **30**, 1318-1328. doi:10.1038/onc.2010.518
Thorpe, G. W., Fong, C. S., Alic, N., Higgins, V. J. and Dawes, I. W. (2004). Cells have distinct mechanisms to maintain protection against different reactive oxygen

species: oxidative-stress-response genes. *Proc. Natl. Acad. Sci. USA* **101**, 6564-6569. doi:10.1073/pnas.0305888101

Twig, G., Elorza, A., Molina, A. J. A., Mohamed, H., Wikstrom, J. D., Walzer, G., Stiles, L., Haigh, S. E., Katz, S., Las, G. et al. (2008). Fission and selective fusion govern mitochondrial segregation and elimination by autophagy. *EMBO J.* **27**, 433-446. doi:10.1038/sj.emboj.7601963

Valm, A. M., Cohen, S., Legant, W. R., Melunis, J., Hershberg, U., Wait, E., Cohen, A. R., Davidson, M. W., Betzig, E. and Lippincott-Schwartz, J. (2017). Applying systems-level spectral imaging and analysis to reveal the organelle interactome. *Nature* **546**, 162-167. doi:10.1038/nature22369

Wagenaar, D. A. (2012). An optically stabilized fast-switching light emitting diode as a light source for functional neuroimaging. *PLoS ONE* **7**, e29822. doi:10.1371/journal.pone.0029822

Wäldchen, S., Lehmann, J., Klein, T., van de Linde, S. and Sauer, M. (2015). Light-induced cell damage in live-cell super-resolution microscopy. *Sci. Rep.* **5**, 15348. doi:10.1038/srep15348

Weigert, M., Schmidt, U., Boothe, T., Müller, A., Dibrov, A., Jain, A., Wilhelm, B., Schmidt, D., Broaddus, C., Culley, S. et al. (2018). Content-aware image restoration: pushing the limits of fluorescence microscopy. *Nat. Methods* **15**, 1090-1097. doi:10.1038/s41592-018-0216-7

Willems, P. H. G. M., Rossignol, R., Dieteren, C. E. J., Murphy, M. P. and Koopman, W. J. H. (2015). Redox homeostasis and mitochondrial dynamics. *Cell Metab.* **22**, 207-218. doi:10.1016/j.cmet.2015.06.006

Zaidel-Bar, R., Ballestrem, C., Kam, Z. and Geiger, B. (2003). Early molecular events in the assembly of matrix adhesions at the leading edge of migrating cells. *J. Cell Sci.* **116**, 4605-4613. doi:10.1242/jcs.00792